This is the author's version of an article that has been published in this journal. Changes were made to this version by the publisher prior to publication.
The final version of record is available at http://dx.doi.org/10.1109/JLT.2020.2989618

Microwave Photonics for Remote Sensing: from Basic Concepts to High-Level Functionalities

G. Serafino, S. Maresca, C. Porzi, F. Scotti, P. Ghelfi, and A. Bogoni

***Abstract*— In the last decades, photonic technologies have been increasingly proposed for microwave and millimeter-wave applications, opening the way to the development of a new field of research known as Microwave Photonics. The hybridization of the microwave world with photonics has demonstrated a beneficial impact on both communications and remote sensing. 5G radio access networks, as well as the next-coming generation of distributed, multistatic radars, are expected to massively leverage on photonic techniques for the generation, distribution, processing, and acquisition of microwave signals. This is due to the advantages brought about by photonics in terms of system transparency to the employed frequency or waveform, low losses, electromagnetic interference immunity, high signal stability. In particular, the inherent coherence guaranteed by photonics will enable next-future multiple input-multiple output radars with enhanced performance. In this paper, we expose in detail some of the most widely employed functions on RF signals obtained with photonic techniques, highlighting the achievable performance that help overcoming some limitations of classical electronic technologies. Finally, two recently implemented microwave photonics systems are described, i.e., a multiple input-multiple output radar and a RF spectrum scanner, showing with practical examples all the potential of microwave photonics systems.**

***Index Terms*—Microwave Photonics; Remote Sensing; MIMO Radar.**

I. Introduction

MICROWAVE photonics (MWP) is a hybrid discipline that bridges applications related to radiofrequency (RF) signals to photonic processing techniques [1]. The history of MWP began few decades ago, when the advances in optics made clear the huge advantages of a hybridization of electronic systems with photonics, initially in terms of low propagation losses and extremely high information transmission capacity. This progressive cross-fertilization revealed favorable for both the RF and the photonic worlds since, on one hand, it allows microwave systems achieving unprecedented performance, for example in terms of high signal purity, large bandwidth (BW), reduced sensitivity to electromagnetic interference (EMI), and better flexibility; on the other hand, it drives an intense research in the field of photonics, pushing it to higher levels of technological maturity, also thanks to always growing industrial investments and market demands.

This work has been submitted on 01 March 2020. It was supported in part by the projects NATO SPS SOLE (G5267), H2020 COST (CA16220), and H2020 SPACEBEAM (#870421).

The first MWP applications became possible thanks to advances in the fabrication of semiconductor lasers [2], photodiodes (PDs) [3], and optical fibers [4]; then, the development of electro-optical modulators (EOMs) [5] helped overcoming the limitations posed by laser direct modulation. All these represent the basic building blocks of a MWP system. Photonics started penetrating the RF world with applications related to signal distribution [6] and true-time delay (TTD) for phased-array antennas (PAAs) [7]. Gradually, other RF functions started being implemented using optical or opto-electronic devices; today, it is possible to efficiently operate not only signal distribution [6], [8]-[12], but also analog-to-digital conversion [13]-[22], frequency conversion/signal mixing [23]-[28], pure oscillations generation [29]-[34], filtering [35]-[45], beamforming [46]-[55], just to number some functionalities.

The development of photonic integrated technologies has recently known a great leap forward [56]-[60]. Photonic integrated circuits (PICs) are, nowadays, mature enough to push to a higher level the performance of MWP systems, also increasing reliability and mechanical robustness, at the same time decreasing size, weight, power, and cost (SWaP-C). Indeed, microwave and mm-wave systems of the next future will be more demanding, not only in terms of performance, but also in terms of SWaP-C. In addition, adaptivity, intended as the capability of dynamically allocating resources and adapting to a changing environment, will be largely sought. These will be, for example, the requirements for communications, driven by the deployment of fifth-generation (5G) networks, as well as for many remote sensing applications, like multiple input-multiple output (MIMO) radar networks [61]-[63].

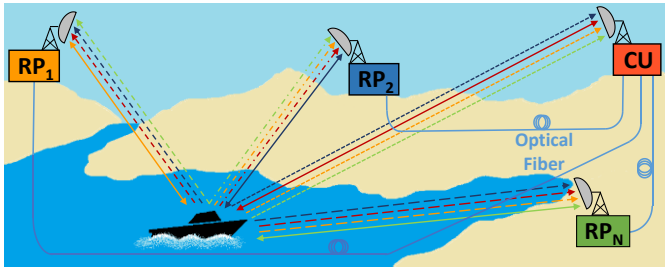

Fig. 1: Elementary scheme of a radar network, exploiting the multistatic approach. Every RP transmits its signal and receives the back-scattered echoes of its own signal and of all the other RPs. RP: radar peripherals; CU: central unit.

G. Serafino, S. Maresca, C. Porzi, and A. Bogoni are with Scuola Superiore di Studi Universitari e di Perfezionamento Sant'Anna, via G. Moruzzi 1, Pisa, 56124, Italy (corresponding author e-mail: g.serafino@santannapisa.it).

F. Scotti and P. Ghelfi are with Consorzio Nazionale Interuniversitario per le Telecomunicazioni (CNIT), via G. Moruzzi 1, Pisa, 56124, Italy.

Copyright (c) 2020 IEEE. Personal use is permitted. For any other purposes, permission must be obtained from the IEEE by emailing pubs-permissions@ieee.org.

This is the author's version of an article that has been published in this journal. Changes were made to this version by the publisher prior to publication.
The final version of record is available at http://dx.doi.org/10.1109/JLT.2020.2989618

The field that could especially benefit from the development of MWP systems and subsystems is remote sensing. Indeed, the branching of remote microwave sensing into several everyday application fields is increasing every year, demanding for distributed radar systems able to collect the most complete information about the scene under observation [64]. In autonomous driving and collision avoidance systems, in air and sea traffic surveillance scenarios, in systems for border control, as well as in medical imaging and environmental monitoring applications, distributed, multistatic radars are increasingly proposed to supersede the idea and performance capabilities of stand-alone, monostatic systems, evolving into the concept of radar networks [65]-[67]. This new generation of complex radar systems is generally composed of a number of radar peripherals (RPs), all connected in a star network configuration to a central unit (CU), as shown in Fig. 1. Each node can be equipped with a transmitter (TX), and with a receiver (RX) that can receive the echoes back-scattered by a target, caused by the waveforms transmitted by any node, following the multistatic approach [68]-[70]. This spatial diversity allows observing the same target or scenario from multiple viewpoints, enhancing the system sensitivity, together with its robustness to target radar cross section (RCS) fluctuations, with the possibility of detecting also very low-RCS or stealth targets [70]. The acquired radar echoes are then sent to the CU, where a joint processing allows extracting a huge amount of information. Moreover, the performance can be further increased employing waveform and frequency diversity, i.e. transmitting different signals on different bands [71]. However, it is fundamental to underline here that the introduced diversity can lead to a gain in the system performance only if all the waveforms transmitted from the different nodes are coherent. Otherwise, the time-alignment of the acquired data can be very hard to obtain with electronic technologies, at the expenses of a heavy signal processing that can introduce a very large computational delay. From the implementation of the first demonstrator of a photonics-assisted radar [72], MWP demonstrated the possibility of joint generation of multiple waveforms, on multiple bands, and their distribution and acquisition, inherently guaranteeing the needed level of coherence, enabling MIMO, i.e. coherent multistatic radar systems [73]-[80].

In this tutorial paper, we present a general overview of some of the most frequently employed MWP techniques and schemes that implement the main functionalities required by microwave and millimeter-wave systems. In Section II, the basic concepts of MWP are exposed, showing how distribution with electro-optical (E/O) and opto-electrical (O/E) conversion, frequency conversion, sampling, filtering, and beamforming of RF signals can be obtained thanks to photonics, with examples about the achievable performance, showing the attainable level of coherence. The reported examples are physically implemented MWP subsystems, often realized by PICs. Then, Section III reports two relevant examples of demonstrators of MWP-based systems that have been recently realized leveraging on photonics for implementing some of the functionalities described in Section II. The last section briefly summarizes the paper content.

II. Microwave Photonics Basics

Referring to the basic scheme reported in Fig. 2 a), any MWP system can be conceived as a three-port network: one optical input, one electrical input, and one electrical output. The main building blocks of a system based on external modulation are essentially four: an optical source, i.e. a single- or multi-wavelength laser, or a subsystem capable of generating an optical frequency comb (OFC) [82], [83]; a device to transfer an electrical signal to the optical domain, often implemented by an EOM; a generic block implementing a certain function on the signal (e.g., simple signal distribution, frequency conversion, sampling, filtering, delay/phase shift); eventually, a PD that transduces the optically processed signal back to the electrical domain. These blocks can be distributed over long distances, instead of been co-located, as usually happens with electronic systems.

In the following, at each wavelength λ (measured in nm) corresponds an optical frequency $\nu = c/\lambda$, (measured in Hz), where c is the speed of light in vacuum. In this paper, for the sake of notation compactness in the equations, we will employ optical angular frequencies $\Omega_x = 2\pi\nu_x$ and electrical angular frequencies $\omega_x = 2\pi f_x$ (where f_x is the frequency measured in Hz), measured in rad/s, and we will refer to quantities Ω or ω simply as frequencies. Uppercase letters will refer to optical frequencies (in the order of hundreds of THz), whereas lowercase letters will refer to lower frequencies (in the range from few MHz to many tens of GHz).

A. Electro-optical Conversion and Signal Distribution

Undoubtedly, Radio-over-Fiber (RoF) links represent one of the most important examples of the penetration of photonics in the microwave world. With respect to classical distribution of

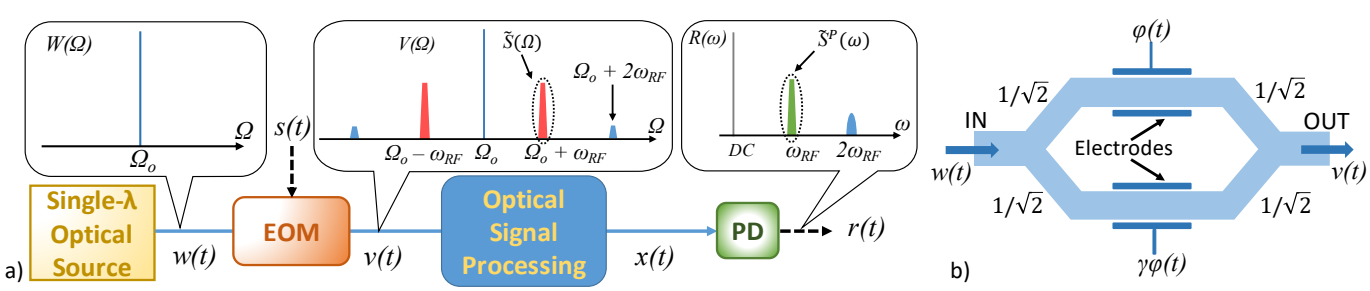

Fig. 2: a) Scheme of a basic MWP system with a single-λ optical source. The insets show how the signal spectrum (optical before the PD, electrical after the PD) changes throughout the system. The Optical Signal Processing Block can represent the distribution, frequency conversion, sampling, filtering, or beamforming functionalities. $\tilde{S}^P$ is the RF input signal after processing; b) Sketch of a typical electro-optical modulator (EOM), a dual-drive Mach-Zehnder intensity modulator.

Copyright (c) 2020 IEEE. Personal use is permitted. For any other purposes, permission must be obtained from the IEEE by emailing pubs-permissions@ieee.org.

This is the author's version of an article that has been published in this journal. Changes were made to this version by the publisher prior to publication.
The final version of record is available at http://dx.doi.org/10.1109/JLT.2020.2989618

signals over copper cables, they offer many advantages: much broader BW, extremely lower attenuation, weight and cost, as well as EMI immunity. RoF links have been considered an optimal solution for the distribution of 5G broadband signals, especially in the millimetre-wave band, but also for microwave signals in the emerging MIMO radar networks.

The first step into a MWP system consists in the E/O conversion of an electrical signal to the optical domain. Fig. 2 a) depicts a RoF link with direct detection (DD), where a single PD is employed, capable of photodetecting the envelope of the received optical signal. RoF links with DD are widely used, and commercial implementations are already available with BW up to 40 GHz. Let us consider a single wavelength (single-λ) optical source, like a continuous-wave laser (CW), whose output *w(t)* is an optical electromagnetic field oscillating at frequency Ω_o. Typically, since the most common lasers in optical communications work in the optical C band, (λ ranging from 1527 to 1560 nm, $\Omega_o \sim 200$THz). Ideally, the optical spectrum $W(\Omega)$ of *w(t)* is a Dirac delta centered in Ω_o, as sketched in the inset of Fig. 2 a):

$$w(t) = Ae^{-j\Omega_o t} \overset{FT}{\leftrightarrow} W(\Omega) = A\delta(\Omega - \Omega_o), \qquad (1)$$

where FT represents the Fourier Transform operation.

Referring to Fig. 2 a) and b), the electrical signal *s(t)* is fed into the EOM, which allows for the E/O conversion of *s(t)*. The most widely employed EOM is the Mach-Zehnder modulator (MZM) [5], [84]. In the MZM, the optical input is split over to equally long waveguides, whereas the electrical input is employed to change the refractive index of one arm with respect to the other, thus differently modulating the phase of the optical signal on each MZM arm. Eventually, the two phase-modulated optical signals recombine, and the resulting signal is modulated in amplitude. In Fig. 2 b), considering for simplicity a perfectly balanced dual-drive EOM [84], the output *v(t)* can be expressed as:

$$v(t) = w(t)\left[e^{j\frac{\pi}{V_\pi}\varphi(t)} + e^{j\gamma\frac{\pi}{V_\pi}\varphi(t)}\right], \qquad (2)$$

where $\varphi(t) = V_b/2 + s(t)/2$, V_π is the modulator half-wave voltage, V_b the bias voltage, and γ is a coefficient that depends on the MZM operation mode. For analogue applications, the EOM is usually driven in its linear region, i.e. biasing it in the middle between the maximum and the null of its cosinusoidal transfer function, with an electrical signal amplitude swing smaller than V_π [84]. This can be obtained by operating the MZM in push-pull mode, i.e. $\gamma = -1$, and setting $V_b = V_\pi/2$.

Let the microwave signal *s(t)* be a radiofrequency signal, with a BW *B*, i.e. a signal with a complex envelope $\tilde{s}(t)$, modulating an oscillation at a given RF frequency ω_{RF}, usually with values ranging from few MHz to some GHz:

$$s(t) = \Re\{\tilde{s}(t)e^{-j\omega_{RF}t}\}, \qquad (3)$$

where $\Re\{\cdot\}$ represents the real part operator. Let us consider, for the sake of notation simplicity, $\tilde{s}(t)$ to be real. Therefore, the MZM output becomes:

$$v(t) = w(t)e^{j\frac{\pi}{4}}\left[e^{j\frac{\pi}{2V_\pi}\tilde{s}(t)\cos(\omega_{RF}t)} + e^{-j\frac{\pi}{2V_\pi}\tilde{s}(t)\cos(\omega_{RF}t) - j\frac{\pi}{2}}\right]. \qquad (4)$$

If $\tilde{s}(t)$ would be complex, the only difference in (4) would be the presence of both I and Q components of the RF signal; therefore, the hypothesis of a real $\tilde{s}(t)$ does not cause any loss of generality. Assuming the amplitude of $\tilde{s}(t)$ small, it is possible to consider the Maclaurin expansion of the exponential function, stopped at the first order, $e^x \cong 1 + x$, so that:

$$v(t) \cong w(t)e^{j\frac{\pi}{4}}\left\{1 + j\frac{\pi}{2V_\pi}\tilde{s}(t)\cos(\omega_{RF}t) - -j\left[1 - j\frac{\pi}{2V_\pi}\tilde{s}(t)\cos(\omega_{RF}t)\right]\right\},$$

which becomes, after simple mathematics,

$$v(t) \cong \sqrt{2}w(t)\left[1 - \frac{\pi}{2V_\pi}\tilde{s}(t)\cos(\omega_{RF}t)\right]. \qquad (5)$$

Applying the FT to (5), we obtain the spectrum of the EOM output, $V(\Omega)$, which is qualitatively sketched in an inset of Fig. 2 a). It is composed by a carrier (central blue line), and two sidebands (SBs) (in red), spaced $\pm\omega_{RF}$ from the optical carrier, whose amplitude is:

$$V(\Omega) = \sqrt{2}A\delta(\Omega - \Omega_o) - -\frac{\pi}{2V_\pi}\frac{A}{\sqrt{2}}\left[\tilde{S}(\Omega - \Omega_o - \omega_{RF}) + \tilde{S}(\Omega - \Omega_o + \omega_{RF})\right]. \qquad (6)$$

$\tilde{S}(\Omega)$ represent the FT, i.e. the spectrum, of the modulating RF signal. It is worth noticing that, if the modulating RF signal is not small, the approximation of the exponential function to the first order does not hold anymore, and other terms must be counted, i.e. $e^x \cong 1 + x + x^2 + x^3 + \cdots$, giving rise to higher-order harmonics. Typically, they appear in (6) as additional SBs at $\Omega - \Omega_o \pm 2\omega_{RF}, \Omega - \Omega_o \pm 3\omega_{RF}$, and so on. As an example, possible two small second-harmonic SBs (in light blue) are reported in the central inset of Fig. 2 a). In the case of a MZM, to understand how "small" is *s(t)*, its amplitude must be compared to the modulator V_π, since the response of a MZM is linear in a range smaller than V_π [84]. Moreover, by properly setting the value of V_b, i.e. biasing the MZM around a null of its voltage-power characteristic function, it is possible to obtain a double-sideband (DSB), suppressed-carrier modulation. Finally, by resorting to more complex structures, like a dual-nested MZM, a single-side band (SSB) modulation can be obtained, also with the possibility of suppressing the carrier [84].

After the EOM, *v(t)* is fed into an "Optical Signal Processing" block. This block, indeed, may perform various operations; its output *x(t)* contains $\tilde{s}^P(t)$, which represents the complex envelope of *s(t)* after processing. Now, we consider the function of signal distribution over optical single-mode fiber (SMF). Therefore, the Optical Signal Processing block in Fig. 2 a) represents a span of optical span with a length *L*, that can be tens or hundreds of km. All the operations on optical signals possibly implemented by this block are the object of the next subsections.

Optical fibers interact with propagating optical fields and, depending on the fiber and on the signal properties, they can give rise to linear and non-linear effects. A thorough analysis of all the effects of the SMF on a propagating signal is out of the scope of this work. Here, we mention only linear phenomena like chromatic dispersion (CD) and attenuation. The former consists in a different group velocity for different wavelengths (or frequencies). For commercial SMF, it is reported as *D*,

Copyright (c) 2020 IEEE. Personal use is permitted. For any other purposes, permission must be obtained from the IEEE by emailing pubs-permissions@ieee.org.

This is the author's version of an article that has been published in this journal. Changes were made to this version by the publisher prior to publication.
The final version of record is available at http://dx.doi.org/10.1109/JLT.2020.2989618

measured in ps/nm/km, which means that two wavelengths (frequencies) that are 1 nm apart (125 GHz apart in frequency, if we are considering the C band), accumulate $|D|$ ps of reciprocal delay for each km they travel along the SMF. A typical value is D = +17 ps/nm/km. CD is an undesired effect that can completely distort the signal if D is too high, or the signal BW too broad, or the SMF span too long. However, being a linear impairment, it can be easily mitigated in different ways that we will mention in the following. Therefore, considering that CD is compensated, the signal $x(t)$ is a retarded and attenuated replica of $v(t)$, composed by the optical carrier and the related SBs. Eventually, it is photodetected by a PD, that converts back the signal to the RF domain. The PD implements the square modulus of the input optical signal, producing an output current proportional to its responsivity η. The generated photocurrent maximum frequency is commonly limited by the PD electrical BW, that can range from few tens of MHz to hundreds of GHz, depending on the particular application. Thus, the output of the PD can be calculated as:

$$r(t) = \eta |x(t)|^2 \otimes h(t), \tag{7}$$

$h(t)$ being the PD electrical response, with BW B_{PD}, whereas $\otimes$ is the operator of convolution. Considering the expression of $w(t)$ and of $s(t)$ in (1) and (3), and the attenuation coefficient a, $r(t)$ is the beating of all the spectral contents of $x(t)$ in the PD:

$$r(t) \propto a \left| A e^{-j\Omega_o t} - \frac{\pi A}{4V_\pi} \tilde{s}(t) \left\{ e^{-j(\Omega_o - \omega_{RF})t} + e^{-j(\Omega_o + \omega_{RF})t} \right\} \right|^2$$

from which we obtain, not considering the PD BW:

$$r(t) = \eta a \left\{ \left[A^2 + \left(\frac{\pi A}{2V_\pi \sqrt{2}} \right)^2 |\tilde{s}^P(t)|^2 \right] - \right.$$
$$\left. - \left(\frac{\pi A^2}{V_\pi} \right) |\tilde{s}^P(t)|^2 \cos(\omega_{RF} t) + \left(\frac{\pi A}{2V_\pi \sqrt{2}} \right)^2 \cos(2\omega_{RF} t) \right\}. \tag{8}$$

Therefore, the spectrum $R(\omega)$ of $r(t)$, for positive frequencies is:

$$R(\omega) = \eta a \left\{ \left[A^2 \delta(\omega) + \left(\frac{\pi A}{2V_\pi \sqrt{2}} \right)^2 \left| \tilde{S}^P(\omega) \right|^2 \right] + \right.$$
$$\left. + \left(\frac{\pi A^2}{V_\pi} \right) \tilde{S}^P(\omega - \omega_{RF}) + \left(\frac{\pi A}{2V_\pi \sqrt{2}} \right)^2 \left| \tilde{S}^P(\omega - 2\omega_{RF}) \right|^2 \right\}. \tag{9}$$

whose amplitude is sketched in an inset of Fig. 2 a). In this case, the contribution around ω_{RF} is $s(t)$ after propagation in the fiber, and it can be selected with a filter. The signal around $2\omega_{RF}$ is usually an unwanted signal that can be rejected if $B_{PD} < 2\omega_{RF}$.

Calculating (8), the two optical SBs in $v(t)$ have clearly the same phase since they sum up constructively after beating with the carrier. If the CD in the RoF link is not negligible, the two SBs travel with different velocities since they are $2\omega_{RF}$ away from each other. This means that, if CD is not compensated, they arrive at the PD with different phases, so that their beat products with the carrier do not sum exactly in phase, reducing the power of the desired signal. However, CD can be easily mitigated by inserting a spool of dispersion compensating fiber (DCF), i.e. a SMF with a CD of opposite sign and proper length, or it can be completely avoided if one of the SBs is canceled, e.g. by an optical filter, or if SSB modulation is employed.

The performance of an analog RoF link are characterized by the same parameters used for RF systems, namely gain G, RF BW, noise figure (NF), spurious-free dynamic range (SFDR), [6], [9]. In these systems, the main source of noise is the laser relative intensity noise (RIN), and the noise already associated with the input RF signal, which can be amplified or not before the EOM. Other limiting factors for the performance of such a system, beyond CD and optical non-linear effects arising in the signal propagation in the fiber, are EOM nonlinearities (i.e. related to its limited linearity or to the stability of the bias working point), and PD saturation. The main figures of merit of a RoF link can be calculated as [6]:

$$G = \eta \frac{\pi}{V_\pi} \bar{P}_R R \tag{10}$$

$$NF = \frac{2}{kTR} \left(\frac{V_\pi}{\pi} \right)^2 \left(\frac{h\omega_{RF}}{\bar{P}_R} \right) \tag{11}$$

$$SFDR = \frac{2}{3} (IIP3 + 174 - NF - 10 log B), \tag{12}$$

where $\bar{P}_R$ is the mean received power, R is the PD load resistance (typically 50 Ω), k is the Boltzmann's constant, T the operation absolute temperature, h the Planck's constant, IIP3 the input third-order intercept, and B the link RF BW which, in the absence of other electronic components, is the narrowest between B_{PD} and the EOM BW.

Although out of the scope of this paper, it is worth mentioning RoF systems with coherent detection, since they offer potentially improved performance. Indeed, they exploit a coherent local oscillator (LO) at the receiver, and PDs in balanced configuration. Thus, they allow recovering also the signal phase, allowing the implementation of sophisticated signal processing functionalities. It was analytically demonstrated that they offer superior performance when compared with DD-based systems in terms of signal-to-noise ratio (SNR) and SFDR [8]. The improved performance is mainly due to the coherent gain and to the balanced detection that allows cancellation of intensity common mode noise. However, a major challenge in the implementation of this kind of RoF links lies in the receiver structure, since they require a coherent receiver with a phase-locked LO with the optical carrier of the RF signal.

B. Photonic Up-conversion and Carrier Generation

To continue investigating more MWP functionalities, let us consider a more generalized scheme of a MWP system, as reported in Fig. 3, with the sketches of the spectra of the signals as they evolve interacting in the system. Here, for generality, we consider a multi-wavelength (multi-λ) or multi-frequency optical source, i.e. a source of many optical oscillations each with a different wavelength (or frequency). Therefore, the optical source output, in the frequency domain, can be expressed as:

$$W(\Omega) = \sum_{k=-K}^{K} p_k \delta(\Omega - \Omega_o + k\omega_r), \tag{13}$$

where p_k are coefficients that determine the shape of the spectrum, with decreasing values as the index k increases in absolute value; Ω_o is the spectrum central frequency, and ω_r is the comb lines spacing. K is an integer number, and the comb has $2K+1$ non-zero amplitude lines. Depending on the specific optical source, the 3dB-bandwidth of $W(\Omega)$ can range from few tens to hundreds of GHz. The comb spectrum representing $W(\Omega)$ is depicted in Fig. 3. By applying the inverse FT to (13), we obtain the source signal in the time domain:

Copyright (c) 2020 IEEE. Personal use is permitted. For any other purposes, permission must be obtained from the IEEE by emailing pubs-permissions@ieee.org.

This is the author's version of an article that has been published in this journal. Changes were made to this version by the publisher prior to publication.
The final version of record is available at http://dx.doi.org/10.1109/JLT.2020.2989618

$$w(t) = \sum_{k=-K}^{K} p_k e^{-j(\Omega_o - k\omega_r)t}. \quad (14)$$

Let us consider now an electrical signal *s(t)*, which is formally identical to the one expressed by (3), but at a lower intermediate frequency (IF) ω_{IF}. Therefore, by applying formulas (2) – (5) with the same assumptions to this optical source, we obtain the spectrum of the EOM output, *V(Ω)*:

$$V(\Omega) = \sqrt{2} \sum_{k=-K}^{K} p_k \Big\{ \delta(\Omega - \Omega_o - k\omega_r) - \frac{\pi}{4V_\pi} \times \big[\tilde{S}(\Omega - \Omega_o - k\omega_r - \omega_{IF}) + \tilde{S}(\Omega - \Omega_o - k\omega_r + \omega_{IF})\big]\Big\}, \quad (15)$$

with the only fundamental difference of having more optical carriers. Indeed, the obtained spectrum, centered again around Ω_o, is composed by lines spaced by ω_r, represented by the Dirac functions; each line has an upper sideband (USB) and a lower sideband (LSB), respectively $+\omega_{IF}$ and $-\omega_{IF}$ away. The assumption of driving the MZM in its linear region, with a small amplitude $\tilde{s}(t)$, allows again the approximation of the exponential function, i.e. only first-order SBs are considered. This is qualitatively illustrated in Fig. 3: a picture of the whole optical spectrum *V(Ω)* is reported, with the comb lines in light blue and the SBs in red, between the lines. A zoom on the spectrum is shown in the inset A: to each line, centered at frequency $\Omega_o + k\omega_r$, corresponds a pair of SBs at $\Omega_o + k\omega_r \pm \omega_{IF}$. Since *w(t)* is composed by $2K+1$ lines, *v(t)* contains $2 \times (2K+1)$ replicas of *s(t)* at frequencies $\Omega_o + k\omega_r \pm \omega_{IF}$.

Here too, after the EOM, *v(t)* is fed into an "Optical Signal Processing" block and, applying (7), the PD output can be approximately expressed as follows:

$$r(t) \simeq 2\eta a \sum_{n=0}^{2K} \Bigg\{ \sum_{k=-K}^{K+1-n} p_k p_{k+n}^* \cos(n\omega_r t) + + \frac{\pi}{V_\pi} \tilde{s}^P(t) \sum_{k=-K}^{K+1-n} p_k^* \cos(n\omega_r t + \omega_{IF} t) \Bigg\} \quad (16)$$

Here, we are considering all the terms given by the line-lines, and line-SBs beatings in the spectrum of *V(Ω)*, neglecting unwanted 0-frequency (DC) components, and all the other beat products which are usually much weaker. Moreover, assuming for simplicity a B_{PD} larger than the higher frequency content in *x(t)*, i.e. $B_{PD} \geq (K-1)\omega_r + \omega_{IF}$, and considering only positive frequencies, the spectrum at the PD output is:

$$R(\omega) = \sum_{n=0}^{2K} \Bigg\{ \sum_{k=-K}^{K+1-n} p_k p_{n+k}^* \delta(\omega - n\omega_r) + + \frac{\pi}{V_\pi} \sum_{k=-K}^{K+1-n} p_k^* \tilde{S}^P(\omega - n\omega_r - \omega_{IF}) \Bigg\}. \quad (17)$$

This electrical spectrum is qualitatively depicted in Fig. 3, where lines spaced by ω_r are shown in grey and their SBs in green. Inset B represents a zoom on the spectrum from DC, and the electrical frequency is represented by ω. In the inset, in light blue, also the neglected terms arising from SB-SB beatings are depicted. Since each SB in *r(t)* represents a replica of the processed signal $\tilde{s}^P(t)$ at a different frequency, it is possible to select one them. For example, if the PD output must be transmitted as a wireless signal at the RF frequency $\omega_{RF} = N\omega_r + \omega_{IF}$, where *N* is an integer, it can easily be done by cascading the PD with an electrical filter with central frequency ω_{RF} and BW *B*. In Fig. 3, inset B, the blue dotted line that sketches the amplitude response of such a band-pass filter (BPF) is depicted around the selected SB. This way, even if the OFC is discrete, by properly setting IF, it is possible to simply up-convert the IF signal *s(t)* at *almost any* desired frequency lower than $\min\{(K-1)\omega_r + \omega_{IF}, B_{PD}\}$, generating signals at the desired carrier frequency. Usually, OFCs allow generating extremely high RF frequencies, up to hundreds of GHz, and the limitations come rather from EOM or PD electrical BWs. However, it is important to properly choose the line spacing ω_r, the IF, and the RF BW *B*, since they must be set to avoid any overlap between SBs in the spectrum. In general, if the 2nd and

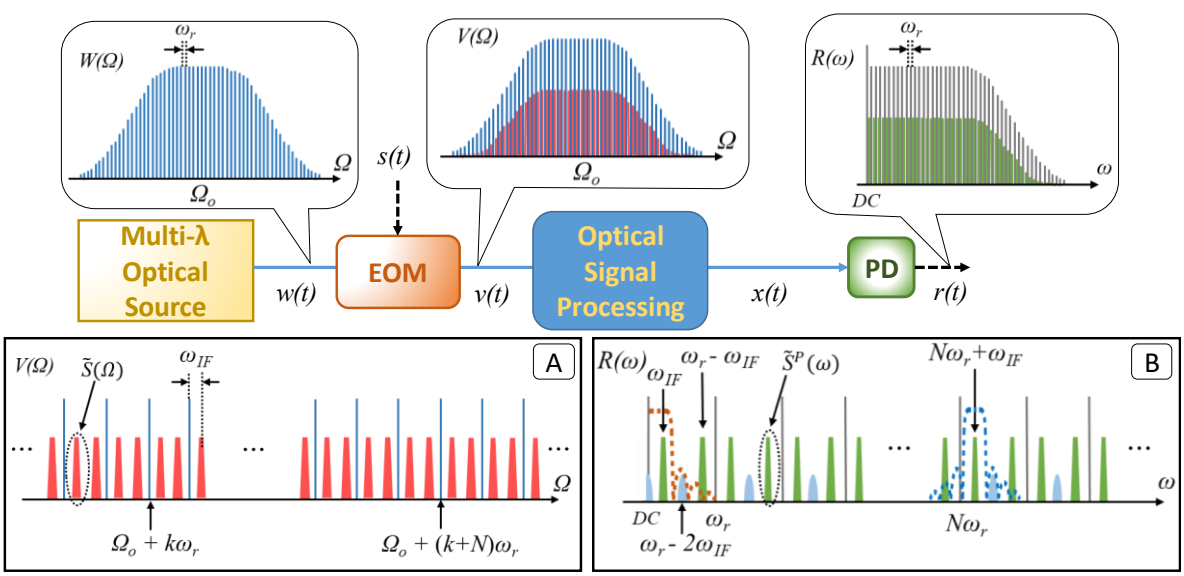

Fig. 3: Scheme of a MWP system with its main building blocks. The spectra of the signal at each stage of the system are qualitatively depicted. Inset A: Zoom on the center of the spectrum of the electro-optically modulated signal. Inset B: Zoom on a part of the spectrum of the photodetected signal, with *N* generic integer. The dashed blue line around $N\omega_r + \omega_{IF}$ represents the amplitude response of a filter that selects that SB for signal up-conversion; a similar amplitude response in dashed red line is at lower frequency for signal down-conversion (in this case, it can be the electrical response of the PD).

Copyright (c) 2020 IEEE. Personal use is permitted. For any other purposes, permission must be obtained from the IEEE by emailing pubs-permissions@ieee.org.

This is the author's version of an article that has been published in this journal. Changes were made to this version by the publisher prior to publication.
The final version of record is available at http://dx.doi.org/10.1109/JLT.2020.2989618

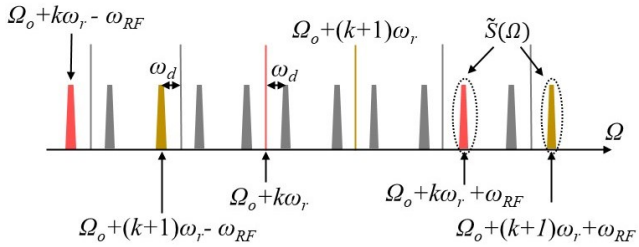

Fig. 4: Effect of the E/O conversion of an RF signal on the spectrum of an OFC. Two generic adjacent lines and their SBs are highlighted in red and yellow. Each line has the related SBs spaced by $\pm\omega_{RF}$.

3rd harmonics are negligible, the condition to avoid overlapping is that the highest frequency of the USB related to the $(k\text{-}1)$-th optical mode is lower than the lowest frequency of the lower LSB related to the k-th optical mode. It can be demonstrated with simple calculations that this corresponds to the condition

$$\omega_r > 2\omega_{IF} + B. \tag{18a}$$

C. Photonic Down-conversion and Sampling

The same scheme depicted in Fig. 3, employed for frequency up-conversion, can also be exploited for the dual operation of down-conversion. Indeed, we can consider $s(t)$ as a signal at a high RF carrier frequency ω_{RF} (with values from few to many tens of GHz, generally $\omega_{RF} > \omega_r$), e.g. coming from a receiving antenna. The involved electro-optical processes are the same but, in this case, each line has the associated SBs at a distance $\pm\omega_{RF}$ in the spectrum, as shown in Fig. 4. However, the EOM output signal has a spectrum structure which is identical to $V(\Omega)$, since the k-th comb line will have two closer SBs, at frequency $\Omega_o + k\omega_r \pm \omega_d$, where $\omega_d \triangleq \omega_{RF} \bmod \omega_r$ represents the remainder of the ratio ω_{RF}/ω_r. It is worth noticing that, in this case, condition (18a) simply becomes:

$$\omega_r > 2\omega_d + B. \tag{18b}$$

Thus, after the optical signal processing block, the output of the PD has a spectrum that can be still represented as the sketch reported in inset B of Fig. 3, whose approximated analytical expression is (17), simply replacing ω_{IF} with ω_d. This means that, beyond DC, the lowest frequency component in $R(\Omega)$ is, for $n = 0$, $\tilde{S}^P(\omega - \omega_d)$, centered around ω_d. Usually, ω_d assumes values in the order of an IF, and all the higher-frequency components of the spectrum can be rejected by a filter or by a low-speed PD electrical response, depicted as a dashed brown line in inset B of Fig. 3. Therefore, the high-frequency signal $s(t)$ that entered the EOM is downconverted from ω_{RF} to ω_d and can be acquired by an electrical analog-to-digital converter (ADC). The photonics-assisted down-conversion is operated without any electrical mixer, which usually worsens the signal phase noise (PN), also adding spurious harmonics. Indeed, in the MWP-based approach, the RF signal is received, processed, and can be up- or downconverted, without heavily affecting the signal quality in the conversion. However, different kinds of noise can affect the PN level [85]. The employed laser linewidth is a crucial parameter, since it is due to fluctuations of the laser central frequency, which can be converted in an intensity instability of the optically up- or down-converted RF signal, during the propagation in the MWP link. An extensive and clear exposition of these matters is out of the scope of this paper and can be found in [85]. Here, we are assuming that an optical source is employed, with a narrow enough linewidth to neglect its effects on the signal. It is worth noticing that for the two dual operations the scheme and the involved processes are exactly the same; thus, if a broadband EOM and a fast PD are adopted, the system can become very flexible in terms of frequency and it can be adapted to many different applications (typically, just employing the proper electronic front-end). Furthermore, it is worth remarking the complete flexibility of the MWP approach: it is not only transparent in terms of frequency, but it is also waveform-agile and it can be employed for the generation and reception of multiple frequencies and multiple waveforms, for multiple applications at the same time.

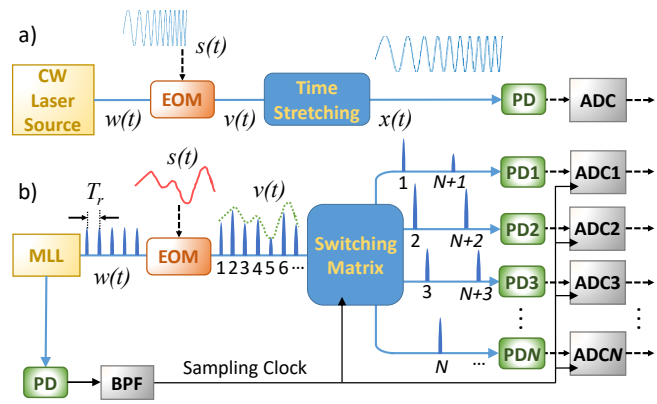

Fig. 5: Two examples of MWP sampling techniques. a) Photonics-assisted sampling with time stretching; b) Optical sampling employing a MLL. The pulse train is amplitude-modulated by the received electrical signal. CW: Continuous wave. MLL: Mode-locked laser; ADC: Analog-to-digital converter; EOM: Electro-optical Modulator; PD: Photodiode.

Considering the system in Fig. 3, it can be also employed for high performance sampling and analog-to-digital (A/D) conversion. Photonics can be employed in A/D conversion in different ways, for instance leveraging on optical sources with very high stability, as opto-electronic oscillators (OEOs) [30], [32], photonics-based frequency synthesizers [33], [34], OFCs [45], [83], and mode-locked lasers (MLLs) [18], [82]. Either the photonics-assisted electronic sampling [13], [21], [86], or the optical sampling [15]-[20], [86], approaches can be considered. Photonics-assisted schemes can be adopted, for example, to improve the aperture jitter of electronic ADCs [14] by generating the system clock from an optical oscillator, e.g. as reported in [86]. Indeed, as shown in the following, the superior phase stability guaranteed by optical sources can significantly enhance the A/D conversion performance. Moreover, photonics allows relaxing the BW requirements of the electronic ADCs employed after photodetection, adding a time-stretching stage, as suggested in [21]. Fig. 5 shows two possible common architectures of A/D conversion operated employing photonics. In Fig. 5 a), the RF signal to be sampled is E/O converted and time-stretched, which is equivalent to shrinking its BW. Here, the optical processing block is represented by the time-stretching operation which, in the optical domain, can be easily implemented, e.g. by CD. Therefore, $x(t)$ is the time-stretched version of $v(t)$. Eventually, $x(t)$ is converted back to the electrical domain and sampled by a low-speed ADC.

Copyright (c) 2020 IEEE. Personal use is permitted. For any other purposes, permission must be obtained from the IEEE by emailing pubs-permissions@ieee.org.

This is the author's version of an article that has been published in this journal. Changes were made to this version by the publisher prior to publication.
The final version of record is available at http://dx.doi.org/10.1109/JLT.2020.2989618

Fig. 5 b) shows an optical sampling scheme employing a MLL. The output of a MLL is train of periodical pulses, with a period T_r. In the time domain, this signal can be expressed as:

$$w(t) = \sum_{k=-\infty}^{+\infty} p(t - kT_r)e^{-j\Omega_o t}, \qquad (19)$$

where $p(t)$ is the pulse shape, and Ω_o is the optical center frequency of the MLL spectrum. Being a periodic signal, $w(t)$ can be written resorting to the Fourier synthesis equation:

$$w(t) = \sum_{k=-\infty}^{+\infty} w_k e^{jk\omega_r t}, \qquad (20)$$

where w_k is the k-th Fourier coefficient and $\omega_r = 2\pi/T_r$ is the pulse repetition frequency. Calculating the expression of a generic w_k by means of the Fourier analysis equation, we obtain:

$$w_k = \frac{1}{T_r}\int_{-\frac{T_r}{2}}^{\frac{T_r}{2}} \sum_{n=-\infty}^{+\infty} p(t - nT_r)\, e^{-j\Omega_o t} e^{-jk\omega_r t} dt = \frac{1}{T_r} P(k\omega_r) e^{-j\Omega_o t}.$$

Here, $P(\omega)$ represents the FT of $p(t)$, which is sampled at every integer multiple of the pulse repetition frequency. Thus, we find for $w(t)$ an expression which is formally identical to (14):

$$w(t) = \frac{1}{T_r} \sum_{k=-\infty}^{+\infty} P(k\omega_r)\, e^{-j(\Omega_o - k\omega_r)t}. \qquad (21)$$

The optical spectrum of this train of pulses is then:

$$W(\Omega) = \frac{1}{T_r} \sum_{k=-\infty}^{+\infty} P(k\omega_r)\, \delta(\Omega - \Omega_o - k\omega_r), \qquad (22)$$

which, again, is formally identical to (13), i.e. the spectrum of a MLL is a comb of lines, spaced by ω_r, whose envelope is given by the FT of the pulse shape. Since a real $p(t)$ has a finite BW, albeit it can span up to hundreds of GHz or 1 THz, the sums in (21) and (22) vanish from a given $|k|$ on. By comparing (13), (14) and (21), (22), we can affirm that, in the frequency domain, a MLL behaves like any OFC. It is worth noticing that, although an OFC looks very much like a MLL, and even if in both cases there is a strong phase locking between the lines in their spectra, the former *is not* a pulsed source. This is because the lines composing their spectra arise from completely different phenomena: the MLL is a multi-mode laser cavity [82], whereas OFCs are generated either by optical non-linear effects in resonators [87] , or by cascading multiple phase and amplitude EOMs [45], [83]. Nowadays, both OFCs and MLLs can be realized in integrated photonic technology [83], [88]. Looking at Fig 5 a), in the time domain, the MLL output is a pulse train that is amplitude-modulated by the RF signal, thus implementing the optical sampling operation, obtaining the signal $v(t)$, whose spectrum is formally identical to $V(\Omega)$ in Fig. 3. This, in turn, means that, if we feed $v(t)$ into a PD, and select at the output the lowest non-zero frequency beating from the spectrum, we just operate an optical down-conversion. Fig. 5 b) also shows how the optically sampled signal can be processed. If the employed MLL has high repetition rate $1/T_r$, the obtained optical signal can be split over N paths, where N-times slower electronic ADCs can be used to quantize the optical pulses after photodetection, and eventually re-interleaved to faithfully reconstruct the signal. In the case of optical sampling, there can be also the possibility of adding time-stretching stages as in [72], relaxing the PD linearity and breakdown threshold constraints. The architectures in Fig. 5 can be, in principle, realized as PICs.

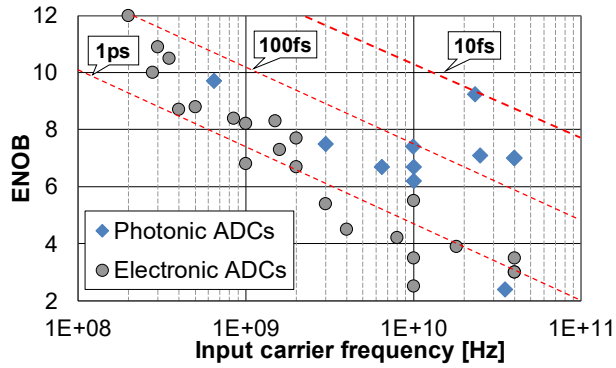

Fig. 6: Walden plot representing the state-of-the-art of ADC technology in terms of ENOB vs. input frequency. Electronic and photonic solutions are reported, together with the limits set by the timing jitter. The best performance (9.24 bits at 23.3 GHz) has been obtained by deep learning network-assisted photonic sampling [22].

The ADC resolution is represented by the effective number of bits (ENOB), which is calculated on the SNR or, more accurately, on the signal-to-noise-and-distortion ratio (SINAD), with the formula [14]:

$$ENOB = \frac{SINAD - 1.76}{6.02}, \qquad (23)$$

where the SINAD is expressed in dB. As a rule of thumb, any increase (or decrease) of the SINAD by 6 dB causes an improvement (or a deterioration) of the ENOB by 1 bit. A crucial role in the performance of any ADC, in terms of ENOB, is the timing jitter of the sampling signal or of the reference sampling clock. Indeed, it significantly contributes to the SINAD. Fig. 6 reports the performance comparison of electronics and photonics solutions [18] and the dashed red lines represent the maximum attainable ENOB at a given frequency, for a fixed time jitter, which represents the upper bound for the ADC resolution. Apparently, the photonics-assisted solutions (represented by the blue squares) overperform the electronic ones.

In (23), all the possible distortions and noises sources are considered; in the case of having timing jitter as limiting source of uncertainty, the ENOB can be determined by [14]:

$$ENOB = \log_2 \frac{1}{\omega_{RF}\delta\tau} - 1 \qquad (24)$$

where $\delta\tau$ is the timing jitter. The main advantage of exploiting optical or photonics-assisted sampling is the extremely low jitter guaranteed by optical sources like OFCs [83] and MLLs [89]. Fig. 7 reports the optical spectra and other features of a MLL and an OFC. The considered fiber MLL has a pulse repetition frequency of ~10 GHz (the exact value is 9.957 GHz), which is the spacing between the lines of the optical spectrum reported in Fig. 7 a), corresponding in wavelength to ~0.08 nm. The MLL electrical spectrum, obtained heterodyning the laser output in a PD, is again composed by 10-GHz spaced modes. The stability of the RF modes is shown in Fig. 7 b), which reports the PN power spectral density (PSD) curves of the MLL electrical spectrum modes from 10 to 50 GHz. The timing jitter

Copyright (c) 2020 IEEE. Personal use is permitted. For any other purposes, permission must be obtained from the IEEE by emailing pubs-permissions@ieee.org.

This is the author's version of an article that has been published in this journal. Changes were made to this version by the publisher prior to publication.
The final version of record is available at http://dx.doi.org/10.1109/JLT.2020.2989618

$\delta\tau$ is calculated as [89]:

$$\delta\tau = \frac{1}{2\pi k f_r}\sqrt{\int_{f_L}^{f_H} S_{\delta\varphi}^{(k)}(f)df}, \qquad (25)$$

where $S_{\delta\varphi}^{(k)}(f)$ is the PN PSD in dBc/Hz of the k-th mode of the MLL electrical spectrum, oscillating at $k\omega_r = 2\pi k f_r$, f is the offset frequency in Hz, i.e. the frequency measured from the carrier kf_r, f_L is the integration lower offset frequency and f_H the integration upper offset frequency. This means that the jitter is obtained by integrating the PN over the range $[f_L, f_H]$, where f_L represents the inverse of the time over which the calculated timing jitter is guaranteed, and f_H is, usually, where the measure enters the thermal noise floor. In other words, $1/f_L$ can be assumed as the mode coherence time. It is possible to demonstrate that the PN PSD scales as $(k\omega_r)^2$ [89]. Moreover, by looking at (25), it is easy to understand that $\delta\tau$ keeps constant for any mode. For this MLL, the measured jitter is 4 fs in the range [5 kHz, 1 MHz], and ~520 fs in [100 Hz, 1 MHz].

The high purity of the RF modes is also witnessed by the SNR ~70 dB lowest-frequency mode at ~10 GHz, shown in Fig. 7 c). The optical spectrum of an OFC with mode spacing of 5 GHz is shown in Fig. 7 d), and the PN PSD corresponding to the first RF mode at 5 GHz is shown in Fig. 7 e). The considered OFC, whose block scheme and picture are reported in Fig. 7 f) and g), has been presented in [83]. It is realized as a monolithic InP PIC containing a distributed Bragg reflector (DBR) laser as optical source, a MZM cascaded with two phase modulators, and a semiconductor optical amplifier (SOA). The red PN curve in Fig. 7 e) is related to the 5-GHz RF mode of the OFC obtained with the DBR laser, and it is compared with the same curve measured employing an external-cavity laser (ECL) as optical source. The black curve represents the back-ground noise. In the worst case (red curve), this OFC exhibits a PN as low as ~95 dBc/Hz at 1 kHz offset frequency.

The here-reported values of timing jitter and PN power demonstrate the excellent performance of these optical sources in terms of signal stability, compared to commercial, state-of-the-art RF electronic oscillators. Indeed, only few electronic technologies can commonly guarantee comparable or better performance, at the expense of frequency tuneability. MLLs and OFCs can help in the generation of highly stable RF carriers, in low-noise RF down-conversion, in the generation of very precise clocks that, in turns, can be exploited for photonics-assisted A/D conversion [13], [86]. MLL pulses, on the other hand, can be exploited for high-precision and frequency-agnostic sampling, guaranteeing high ENOB on a wide range of received RF frequencies, as shown in Fig. 6.

D. Photonic Filtering of Microwave Signals

Filtering is one of the fundamental functions operated on signals. Ideally, the frequency response of a filter with a given BW, defined for a particular application, should be flat in amplitude and linear in phase within the passband, with large attenuation outside it, and infinite roll-off so to have a box-like shape. Additionally, the filter central frequency should be broadly tunable. In the microwave domain, realising filters with sharp edges and broad tuneability is possible, but it becomes really challenging as the signals carrier frequency increases beyond few GHz. Conversely, exploiting photonic technologies, widely tuneable filters for microwave signals can be easily realised, since the obtained fractional BW is extremely small, as the central frequencies are typically in the order of ~ 200 THz, whereas the needed pass-band is few GHz wide, at most. Yet, this demands very high Q factors, which is a challenge for MWP filters implementation. For this reason, also in the optical domain, filters are often based on resonant structures [38]-[44], [91], even though they can only approximate linear phase response within the passband.

We can refer again to the scheme in Fig. 2 a), where the electric RF signal is first converted into the optical domain. In this case, the "Optical Signal Processing" block is represented by an optical filter. Therefore, the E/O converted microwave signal is optically filtered, and then O/E converted back to the electrical domain. The optical filter frequency response is such that the same RF filtering operation using electronic devices is obtained for the resulting O/E converted signal.

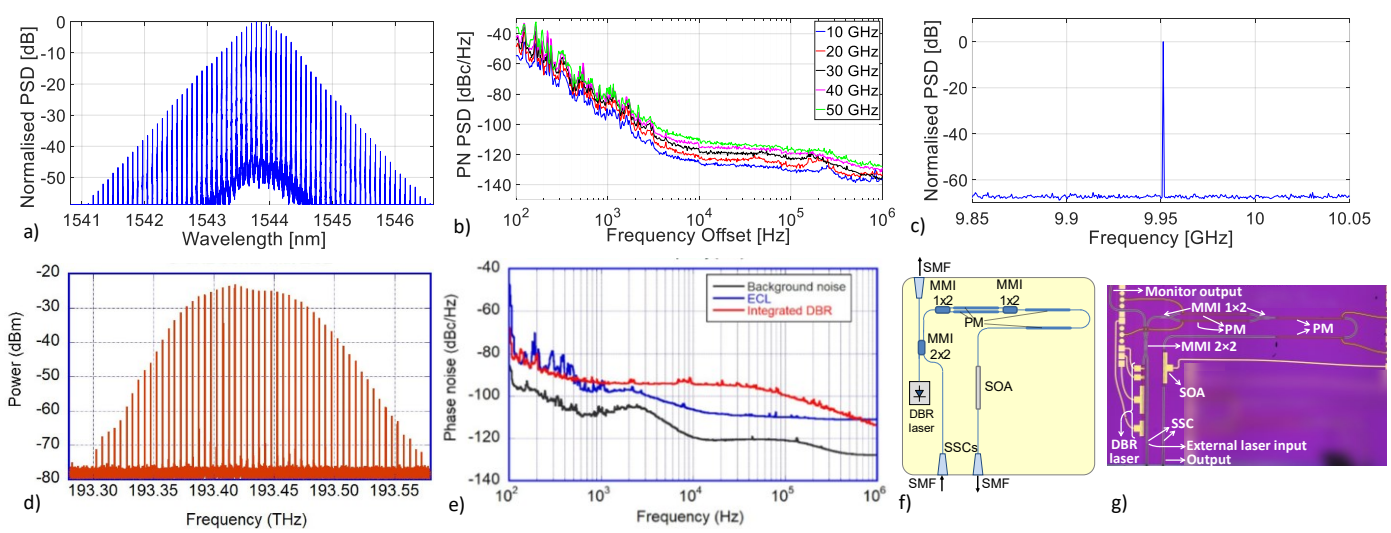

Fig. 7: a) Optical spectrum of a 10-GHz repetition rate MLL; b) Phase Noise (PN) power spectral density (PSD) of the MLL electrical spectrum RF modes, from 10 GHz to 50 GHz [89]; c) Lowest-frequency mode of the electrical spectrum of the same MLL; d) Optical spectrum of a 5-GHz frequency spacing OFC; e) PN PSD of the comb RF fundamental line at 5 GHz, using two different optical sources, namely a distributed Bragg reflector (DBR) laser, and an external-cavity laser (ECL); f) OFC architecture sketch; g) OFC photonic-integrated circuit picture (pictures d – g are a courtesy of N. Andriolli *et al.*, [83]).

Copyright (c) 2020 IEEE. Personal use is permitted. For any other purposes, permission must be obtained from the IEEE by emailing pubs-permissions@ieee.org.

This is the author's version of an article that has been published in this journal. Changes were made to this version by the publisher prior to publication.
The final version of record is available at http://dx.doi.org/10.1109/JLT.2020.2989618

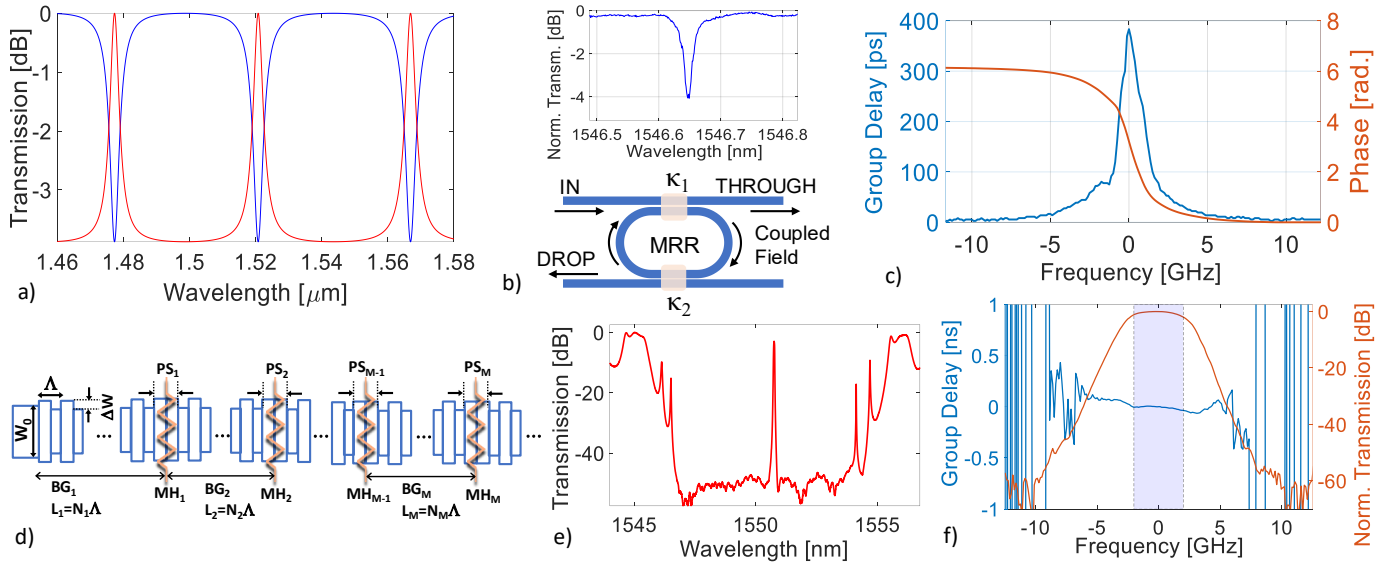

Fig. 8: a) Theoretical example of an optical resonator output (in case of a MRR from drop, red, and through, blue port); b) Optical MRR sketch, with its input and output ports (inset: example of measured THROUGH notch of a Si MRR); c) example of a MRR measured group delay and phase response; d) sketch of a DFBR, composed by multiple Bragg gratings (BGs) with phase shifts (PS), adjusted by micro-heaters (MHs) to compensate for fabrication errors; e) example of a DFBR measured optical transmission response; f) example of a DFBR measured group delay and transmission. The shaded area highlights the 4 GHz-wide 1-dB pass-

MWP filters have been realised with many different approaches and techniques, with bulk [45], [35], [36], or integrated [38]-[44] technologies. Since filters are passive devices for which loss minimization is of paramount importance, the preferred technological platforms are CMOS-compatible, as Silicon-on-Insulator (SOI) and Si_2N_3 (like TriPleX). Lately, filters realised as PICs became particularly attractive, since they can offer *(i)* a high flexibility in terms of frequency response, in amplitude as well as in phase, *(ii)* a good mechanical robustness, *(iii)* a reduced SWaP-C, and *(iv)* the possibility of being easily controlled in temperature. Moreover, they allow the realization of infinite or finite impulse response filters (IIR and FIR, respectively). The latter can be obtained, e.g., by cascading several Mach-Zehnder interferometer (MZI) structures; the former can be implemented resorting to Fabry-Perot interferometers (FPIs) or micro-ring resonators (MRRs) [91]. It has been demonstrated that the frequency response $H(\Omega)$ of any optical filter can be decomposed as [35]:

$$H(\Omega) = \sum_{n=1}^{N} c_n e^{jn\Omega T}\,, \qquad (26)$$

where $c_n = |c_n|e^{j\phi_n}$ are complex coefficients, N is the filter order, and T is a characteristic parameter of the considered filter. For FIR filters, N is a finite number, whereas for IIR filters, $N \to \infty$. The infinite summation is representative of the recirculating nature of the IIR filter, in which properly delayed and weighted replicas of the input signal are summed-up through a feed-back path to give the filter output. As an example, a FPI realizes a resonant cavity between two semi-reflective mirrors (which can also be implemented by the facets of a thin film). The light entering the cavity bounces back and forth between the mirrors, therefore interfering with itself. The resonant wavelengths λ_{res}, meeting the condition

$$m\lambda_{res} = 2l_{opt}, \qquad (27)$$

with m positive integer and l_{opt} the optical length of the cavity, constructively interfere. Consequently, the output transmitted and reflected spectra, which are obtained by the summation of the infinite replicas of the cavity field transmitted through the mirrors, exhibit the typical peaks and notches, respectively, illustrated in Fig. 8 a). For the FPI, $T = 2l_{opt}/c$, i.e. it is the time needed by light to travel the entire cavity. From condition (27), it is easy to understand that the transmission response of the FPI is periodic in wavelength (or frequency); its period is known as free spectral range (FSR), defined as $1/T$. In Fig. 8 a), three FSRs are reported. The narrower the linewidth of a cavity resonance, the highest its Q factor.

A similar behavior is observed for a MRR resonator, whose typical structure is reported in Fig. 8 b) where the input port IN, and the two output ports, THROUGH and DROP, are provided by two bus waveguides placed in proximity of the ring waveguide so that part of the light is coupled in the resonator, being κ_1 and κ_2 the coupling factors, similarly to the partially reflective mirrors of a FPI. For this reason, the same periodic peaks and notches of Fig. 8 a) appear at the DROP and THROUGH port of a MRR, respectively, with the only difference that now $T=l_{opt}/c$, and the FSR doubles in respect to FPI for the same cavity length. In general, Fig. 8 a) represents the theoretical reflection (peaks) and transmission (notches) response of a resonant optical cavity.

The inset in Fig. 8 b) shows the measured transmission notch at the THROUGH port of a single Si MRR. Fig. 8 c) reports the measured group delay (GD, blue curve) and phase (red curve) response of the same MRR, plotted vs. the offset frequency from a resonant frequency. The maximum GD occurs at resonance, in correspondence of the maximum storage time for the field energy, and the phase shows a 2π transition around the notch, showing an almost linear response closely around the resonance. High-order filter response with flat-top feature and sharper roll-off than the Lorentzian shape of Fig. 8 a) can be obtained with a multi-cavity approach and advanced photonic integrated filters can be realized using either coupled MRRs [39] or distributed feedback resonator (DFBRs) [44]. The central wavelength of such integrated optical filters can be tuned by exploiting thermo-optic effect in either Si or Si_3N_4 waveguides.

Copyright (c) 2020 IEEE. Personal use is permitted. For any other purposes, permission must be obtained from the IEEE by emailing pubs-permissions@ieee.org.

This is the author's version of an article that has been published in this journal. Changes were made to this version by the publisher prior to publication.
The final version of record is available at http://dx.doi.org/10.1109/JLT.2020.2989618

An integrated version of a FPI can be realized in a DFBR where the cavity mirrors are implemented through waveguide Bragg gratings (WBGs) [92]. Indeed, Bragg gratings (BGs) are reflective to one wavelength, called Bragg wavelength, being transparent to all the others. Several cascaded FPI can implement a filter with a flat-top shape, with a BW that can be of the order of hundreds of MHz or some GHz, with very sharp edges. Fig. 8 d) shows the scheme of an Mth-order DFBR comprising M+1 sidewall corrugated symmetric WBGs in which the width of a silicon strip waveguide with average value W_0 is periodically varied by ΔW with a corrugation period Λ [39], [44]. In order to compensate for fabrication imperfections, the optical path of the resonant cavities encompassed between the WBG mirrors are locally controlled though resistive micro-heaters (MHs) that allow fairly reconstructing the designed filter response. As an example, Fig. 8 e) shows the transmission spectrum of a narrow-bandwidth 3rd-order DFBR. A sharp transmission window with moderate insertion loss of ~2.5 dB, and an out-of-band rejection of ~50 dB over a 7.5 nm-wide stop-band region is reported. As depicted in Fig. 8 e), the measured filter group delay is almost linear within a 4 GHz-wide 1-dB pass-band [44].

E. Photonic Beamforming

Beamforming (BF) is the capability of an antenna of dynamically changing the pointing direction and the shape of its radiation pattern, without any mechanical movement [90]. BF is applied to phased-array antennas (PAAs), which are composed by many elements fed with a replica of the signal to be transmitted with a different phase and amplitude. By leveraging on the interference between the electromagnetic fields emitted by the elements, it is possible to vary the PAA pointing direction. Let us consider a PAA composed by N elements, equally spaced by a distance d, as shown in Fig. 9 a), where only the first four elements are depicted, and the steering of the radiation pattern main lobe in three possible directions is sketched (0°, -30°, and -60°). For the sake of clarity and simplicity of the exposition, we will consider a special case, represented by uniform PAAs, for which there is a constant phase difference between adjacent elements. This allows exposing the basic principles of beamforming in a rigorous, yet simple way. The reader can refer to [90] for a detailed and general theoretical exposition of PAAs and beamforming.

The maximum direction of the PAA radiation pattern is where the fields radiated by the elements sum up in phase. Considering Fig. 9 a), looking in the direction $\bar{\theta}_s$, the signals from elements 3 and 4 can be in phase if the signal from element 3 starts propagating with the same phase that the signal from element 4 has after propagating on a distance $\Delta x = d \sin \bar{\theta}_s$. By considering the geometry of the problem, this is equivalent to shift the phase of the signal from element 3 by the amount $\Delta\psi$:

$$\Delta\psi = k\Delta x = \frac{2\pi}{\lambda} d \sin \bar{\theta}_s, \qquad (28)$$

where k is the signal wavenumber and λ is its wavelength. In other words, if we want to change the PAA pointing angle to a generic θ_s, the wave fronts of the fields radiated by each element in the far-field region must be tilted by the same angle θ_s, complying with (28). In theory, by properly setting the phase difference between the N elements, it is possible to arbitrarily steer the PAA radiation pattern.

In the case of a uniform PAA, the BF network (BFN) driving its elements sets a phase ψ_i and an amplitude a_i on each of them, with $a_i = 1/N$ and $\psi_i - \psi_{i-1} = \Delta\psi, \forall\, 1 \le i \le N$. The antenna radiation pattern of a PAA is given by the single element pattern multiplied by the array factor AF, obtained as:

$$AF(\theta) = \frac{1}{N}\sum_{n=1}^{N} e^{jn(2\pi\frac{d}{\lambda}\cos\theta - \Delta\psi)}, \qquad (29)$$

where θ is the azimuth. The phase variation $\Delta\psi$ can be obtained either following the true-time delay (TTD) approach, i.e. by setting a different time delay $\Delta\tau$ to the signals emitted by different elements; or with the phase shift (PS) approach, i.e. by shifting their phase. In both cases, the phase of arrival of the signal at each element is different. For a steering angle θ_s, the needed delay $\Delta\tau$ can be obtained recalling that $\Delta\psi = 2\pi f \Delta\tau$, and $f\lambda = c$:

$$\Delta\tau = \frac{d}{c}\sin\theta_s, \qquad (30)$$

where c is the signal propagation velocity. Apparently, such a delay is independent on the signal frequency. Hence, a fixed TTD as in (30) corresponds to a wavelength-dependent (i.e. frequency-dependent) PS, as in (28). In other words, implementing a TTD approach is equivalent to setting a PS proportional to the signal frequency. On the other hand, the PS approach consists in introducing a phase difference between the PAA elements that is *constant* over the *entire* signal BW, rather than linearly varying as in TTD.

Today, in the electronic domain, BFNs driving PAAs are made with analog or digital phase shifters. Analogue phase shifters operate on limited BWs; digital devices may have BWs of some GHz, but they usually do not guarantee the same

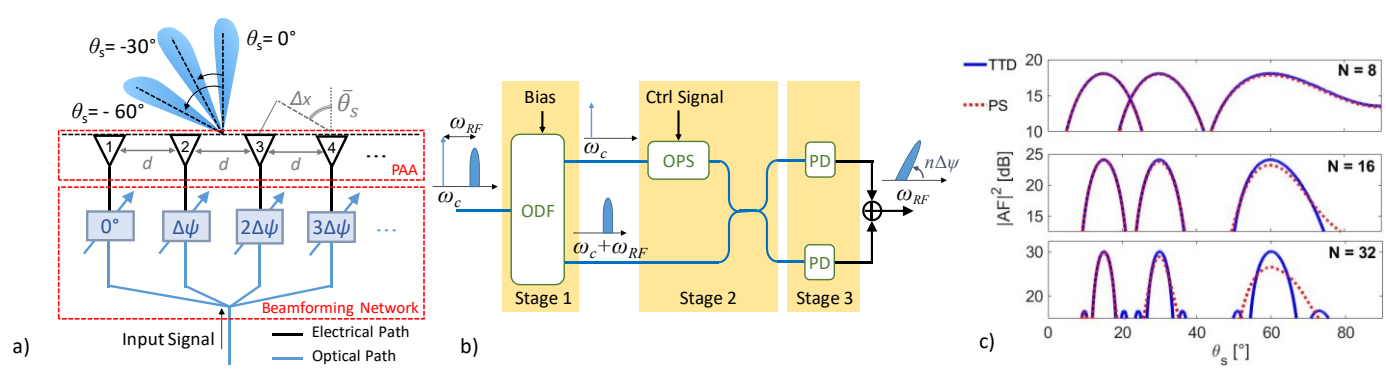

Fig. 9: a) Sketch of the structure of a PAA with its beamforming network; b) Scheme of the architecture of a PS-based BFN element; c) Array gain of a PAA vs. the steering angle in case of 8, 16, 32 elements (top to bottom), for a PS-based (red, dotted line) and a TTD-based (blue, solid line) approach.

Copyright (c) 2020 IEEE. Personal use is permitted. For any other purposes, permission must be obtained from the IEEE by emailing pubs-permissions@ieee.org.

This is the author's version of an article that has been published in this journal. Changes were made to this version by the publisher prior to publication.
The final version of record is available at http://dx.doi.org/10.1109/JLT.2020.2989618

performance for every operating frequency. Moreover, digital devices exhibit coarse phase control and non-negligible phase errors. Electronic digital TTD suffers from the same limitations, whereas TTD it is unpractical with analogue devices. Instead, a photonics-assisted approach makes possible BFN architectures that can be either TTD-based [46]-[48], [53], [54], or PS-based [49]-[52]. To obtain photonics-assisted BF, the RF signal to be transmitted must be E/O converted (with the methods described in subsections II.A and II.B), split over N optical paths to the N PAA elements, and undergo a delay or a PS in a BFN module, as shown in Fig. 9. a). Then, it can be converted back to the RF domain by PDs and transmitted.

To understand how an optical BFN can work, let us consider the case of PS-based BF, in a PAA in transmission mode (the receiving mode is the dual process). Fig 9 b) shows a scheme of an optical phase shifter (OPS). An optical SSB-modulated signal:

$$x(t) = A_c e^{j\omega_c t} + \tilde{s}(t) e^{j(\omega_c + \omega_{RF})t}, \qquad (31)$$

with a modulating signal $\tilde{s}(t)$, a carrier at optical frequency ω_c and a SB at $\omega_c + \omega_{RF}$, enters the optical de-interleaver filter (ODF) of the PAA n-th element. The ODF is a filter with two output arms, capable of routing some frequencies to the upper arm, other frequencies to the lower arm. It can be implemented by a MZI loaded with a MRR [91], that spatially separates the carrier from the SB, routing the carrier to the ODF upper arm, i.e. to the OPS. The carrier is phase-shifted by the desired amount $n\Delta\psi$ and, later, it is recombined with its SB. The signal is eventually heterodyned in a PD, or in two balanced PDs, to minimize losses. The output is the beat of the phase-shifted carrier and its SB, from (7):

$$x_{PD}(t) \sim A_c^2 + |\tilde{s}(t)|^2 + 2\Re\{A_c e^{-j(\omega_c t - n\Delta\psi)} \tilde{s}(t) e^{j(\omega_c + \omega_{RF})t}\},$$

from which, rejecting low-frequency components, we can select the phase-shifted signal to be transmitted:

$$r(t) = A_c \tilde{s}(t) \cos(\omega_{RF} t + n\Delta\psi). \qquad (32)$$

Thus, the PS applied to the optical carrier is transferred to the RF signal that is fed to the PAA element.

The same process is followed if a TTD-approach is implemented, with the fundamental difference that the delay $\Delta\tau$ is applied to the entire SB, instead than on the carrier only. Optical TTD can be effectively obtained exploiting CD in optical fibers or other dispersive media, since different wavelengths travel with different velocities [47], [53], [54], [93]. In general, if D is the CD coefficient (introduced in subsection II.A) and L is the length of a dispersive element, two signals spaced in wavelength by a quantity $\Delta\lambda$, accumulate a reciprocal delay $\Delta\tau$, expressed in ps, given by:

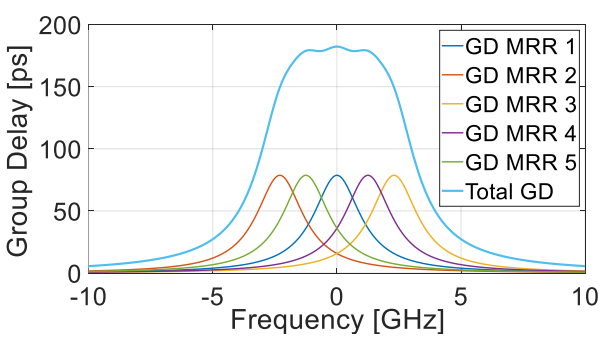

Fig. 10: Theoretical example of the GD of 5 cascaded MRRs that can sum up to obtain a larger GD on a broader BW.

$$\Delta\tau = D \cdot L \cdot \Delta\lambda. \qquad (33)$$

Thus, by modulating a replica of the RF signal on a different carrier wavelength for each PAA element, it is possible to obtain different propagation delays for different elements, in one dimension [47], as well as in two [53], [54]. $\Delta\tau$ can be finely tuned by changing the wavelength of the optical carriers, considering the employed fiber total CD, expressed in ps/nm. The employed tuneable dispersion elements are optical dispersion compensators (ODCs), usually employed for CD management in optical communications. They are based on DCF modules [47], [53], or fiber BGs [54], offering a variable delay to the propagating signal depending on its optical wavelength (or frequency). They allow for a squint-free large beam scanning over very large angles, although fiber-based ODC elements cannot be integrated and can be relatively bulky and with limited tuneability speed. However, similar solutions can become interesting considering the possibility of realizing tuneable ODCs on PICs [93].

MRRs are structures that can be easily realized as PICs, and can be exploited to implement either TTD [46], [48], or PS [50]. As shown in the previous subsection (see Fig. 8 c), the MRR introduces a GD across the central frequency of its notch response: such a GD can be employed to set a time delay to the signal coupled to the ring. TTD must be applied to all the frequency components of the signal, but this may have a too large BW compared to the MRR GD narrow peak. However, if more MRRs are cascaded, and their central wavelengths are properly detuned to slightly misalign their responses, their GDs can sum to obtain a higher, flat-top GD response of the whole cascade with a larger BW, as shown in Fig. 10, where 5 MRRs with a BW < 2 GHz are employed to obtain a GD over > 5 GHz. Optical MRRs give the possibility of realizing also PS, thanks to their linear phase response, as shown in Fig. 8 c) (red curve). Indeed, the signals falling in the MRR notch undergo a phase shift approximately in the range [-π, +π]. Unlike for TTD, the narrow BW of the MRR, here translated to a steep slope of the phase response, is not a big problem, since PS can be applied to the optical carrier only: the PS will be eventually transferred to the carrier-SB RF beat signal at the output of the PD that feeds each PAA element. As it can be seen from Fig. 8 c), the possible PS inside the notch is less than 2π; here, again, it is possible to solve the problem by cascading two MRRs, if a larger PS is needed.

As for filters, if the OPS is realized with a MRR, the applied PS can be changed either by tuning the carrier wavelength on the phase response curve, or by tuning the MRR central wavelength thanks to the thermo-optic effect, which varies the effective index of the resonator with temperature. Laser wavelength tuning and thermo-optic effect can be too slow for some BF applications. Therefore, faster photonic phase shifters can be obtained thanks to the carrier depletion effect, applied to MRRs or to straight waveguides. This effect consists in varying the effective index of *pn*-doped junctions distributed over the waveguide, by changing their bias.

If the considered signal is a pure sinewave, TTD and PS are equivalent. Otherwise, if the signal has a non-zero BW, the PS-based approach applies a flat $\Delta\psi$ over all the frequencies, therefore strictly meeting condition (28) only for the carrier frequency. This can be the cause of the undesired effect of beam squint, consisting in a detrimental distortion of the antenna

Copyright (c) 2020 IEEE. Personal use is permitted. For any other purposes, permission must be obtained from the IEEE by emailing pubs-permissions@ieee.org.

This is the author's version of an article that has been published in this journal. Changes were made to this version by the publisher prior to publication.
The final version of record is available at http://dx.doi.org/10.1109/JLT.2020.2989618

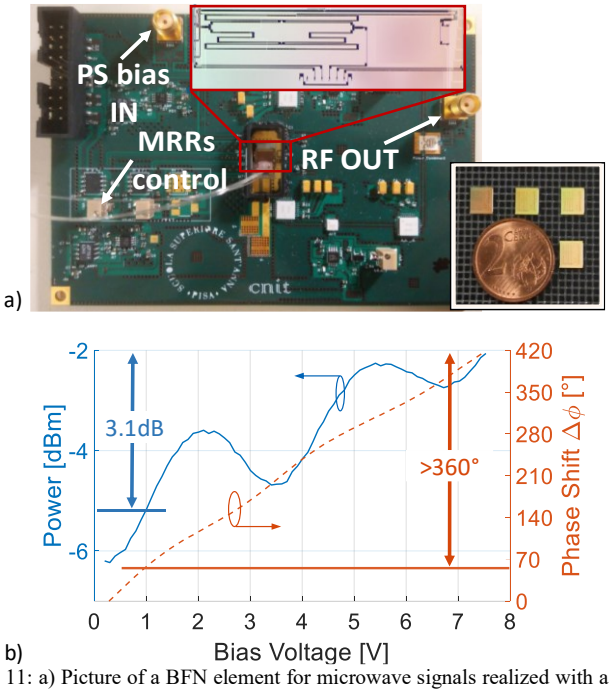

Fig. 11: a) Picture of a BFN element for microwave signals realized with a Si-photonic PIC (Insets: top: the optical phase shifter; side: chips containing each 5 optical phase shifters); b) Power and phase response of the BFN element [52].

pattern, that alters its width and pointing direction. Nevertheless, although photonic TTD represents the best performing solution in terms of operational BW and robustness to beam squint, it is in general quite costly and requires many controls since, as we have shown here, often many MRRs are required for a single BFN element. On the other hand, optical PS also represents a valid solution, since it requires less complex controls, and can operate on a very wide range of frequencies, as long as the squint remains tolerable. The effect of squint is heavier for larger steering angles, larger signal fractional BW, and for a larger number of PAA elements. Fig. 9 c) shows the penalty induced by beam squint in terms of radiation pattern gain vs. the pointing direction. Considering a signal with relatively wide fractional BW ~12.5%, it represents the $|AF|^2$ (i.e. the array antenna gain) integrated on the whole signal BW, in the case of array element number $N = 8$, 16, and 32. TTD and PS performance are compared and, apparently, the penalty starts being non-negligible for $N = 32$ and for $\theta_s \geq \pm 60°$. Therefore, even if the PS approach is not squint-immune, it can represent in many cases a good trade-off between performance and complexity.

A good example of a high-performance PS-based, photonics-assisted BFN, realized in Si-photonics, is reported in [51]-[53], where its suitability to wideband wireless access networks and radar applications is demonstrated. A picture of the electronic board hosting the OPS PIC is reported in Fig. 11 a). The upper inset shows the OPS structure, whereas the lower inset depicts some entire chips, each containing four of those structures, giving an idea of the high level of miniaturization. The OPS section is implemented by a *pn*-doped waveguide, driven in reverse bias condition. By changing the applied bias to modulate the waveguide effective index thanks to the carrier depletion effect, it is possible to obtain a highly linear PS curve on a range >360°, reported in Fig. 11 b) (red, dashed line). A limited power fluctuation, represented by the solid, blue line, is associated to the PS, due to the change of light absorption of the doped waveguide, induced by the index variations.

III. Photonics-Assisted Microwave Systems

This section is dedicated to the description of two examples of sensing systems which massively leverage on photonics for generation, distribution, analogue processing, and acquisition of microwave signals: the demonstrator of a 2 TX x 2 RX MIMO radar, and the prototype of a RF spectrum scanner.

A. Photonics-Enabled Radar Networks

Classical monostatic or bi-static radars are frequently subject to performance limitations due to large random fluctuations of the targets RCS. Moreover, they show poor capabilities of coping with stealth targets, which exhibit a very small RCS to these kinds of system. Conversely, multistatic radars can work following a network-based paradigm, which relies on the broad concept of data fusion by employing multiple distributed radar nodes to monitor a common area of interest, offering enhanced capabilities in observing a scene from multiple viewpoints, thus increasing the system sensitivity, as depicted in Fig. 1. This kind of systems have been theoretically investigated [61], [65], [66], and physically implemented in a number of solutions [67], [68], [76]-[80], to address the increasingly complex operational scenarios and mission demands. MIMO radar systems, a specific subset of distributed multistatic radar networks, are characterized by a deeper degree of cooperation among the radar nodes, which have not only the capability to observe the same scene from different viewpoints, but also to employ multiple coherent transmitted waveforms and to jointly process, in a centralized manner, the signals received by the RPs [61]. Theoretical studies on MIMO radars, especially with widely separated antennas, have highlighted the enormous potential of such systems, their increased flexibility and power efficiency [69], as well as their improved target detection and localization capabilities [62], [63], [70], especially when attempting to detect low-detectable targets or with high angular RCS variability. Interesting implementations of this kind of radar systems has been recently reported in [76]-[80]. All these implementations have in common employing a 2 TX x 2 RX architecture, with centralized processing of the received echoes. The system in [77] is very interesting since it gives the possibility of distinguishing which transmitter originated the backscattered signal, thanks to the discrimination of the transmitted signal polarity. Instead, the main peculiarity of the system proposed in [78] consists in the signal generation: each transmitter is equipped with an independent chaotic OEO, instead of generating the waveform in the central unit, as in [76], [77], [79], [80]. The MIMO systems demonstrated in [77]-[79] are tested in an indoor scenario, showing excellent capabilities in target localization, with errors of few cm. In this work, we are interested in showing, as an example, a MIMO system with widely spaced antennas, tested in an outdoor field.

MIMO radars with widely separated antennas can fully exploit the joint information from all the viewpoints if data do not undergo any processing in the RPs, but are sent raw to the

Copyright (c) 2020 IEEE. Personal use is permitted. For any other purposes, permission must be obtained from the IEEE by emailing pubs-permissions@ieee.org.

This is the author's version of an article that has been published in this journal. Changes were made to this version by the publisher prior to publication.
The final version of record is available at http://dx.doi.org/10.1109/JLT.2020.2989618

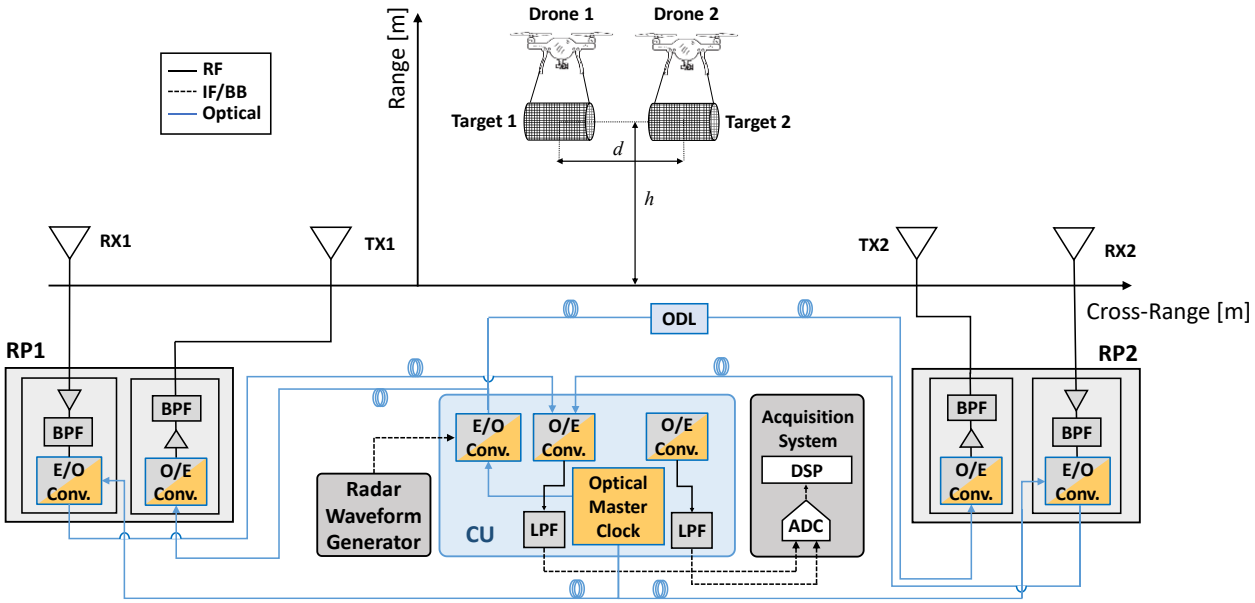

Fig. 12: Architecture of the proposed Photonic Radar Network and geometry of the in-field experimental setup. DSP: Digital Signal Processing; ADC: Analog-to-Digital Converter; RF: Radio Frequency; LPF: Low-Pass Filter; E/O: Electro-Optical; ODL: Optical Delay Line; O/E: Opto-Electrical; IF/BB: Intermediate Frequency/Base Band; BPF: Band-Pass Filter.

CU. In a real operative scenario, this requires *(i)* precise time and phase synchronization between the CU and the RPs, and *(ii)* reliable large-BW, long-range signal distribution among the remote nodes and the CU operating data fusion [73] between the data acquired by all the RPs. In a single word, the nodes must be *coherent*. This is a highly demanding feature for classical electronic systems. On the other hand, photonic technology has the right cards to address these issues, overcoming the actual limitations of electronic devices and subsystems, thanks to the inherent coherence it can guarantee, with functionalities and performance achievements that have been presented in the previous sections. It is worth underlining that, in this context, the term coherence has a double meaning: it can be intended as high stability of the optically generated signals, as well as the time and phase alignment between the CU and the RPs, avoiding complex synchronization mechanisms. Indeed, MWP assures two key features: *(i)* the possibility to generate signals with long-time phase stability and frequency/phase coherence between the TX and RX nodes [73], [81], [89] and *(ii)* possibility to distribute the signals by means of SMF links, maintaining the high-quality/coherence and the needed long-range, large-BW connectivity between the radar network nodes [73], [74].

Here, a centralized distributed MIMO radar demonstrator is described, which relies on photonic technology for the LO and for the peripherals remoting. The first pioneering coherent radar based on photonics [71], together with the experimental results in a maritime surveillance scenario [75], have suggested the possibility to develop the very first, at the best of our knowledge, photonics-based MIMO radar demonstrator in outdoor environments [76], [80]. These experiments have been conducted as preliminary activities for the design and implementation of a fully operational multiband centralized radar network based on photonic technology.

The proposed radar network architecture is depicted in Fig. 12. The system consists of two RPs, each with a TX and a RX, for a total of four coherent virtual channels. The optical master clock is a 400-MHz repetition rate MLL. Optical filters are employed to separate two groups of MLL modes for each RP. The radar waveform is a train of linear frequency modulated (LFM) pulses that are generated at an IF of 100 MHz and E/O converted in the CU, modulating the first group of modes. These modulated optical modes are sent over a spool of SMF to the RPs, together with the second group, which is not modulated. In each RP, the modulated optical signal is employed to upconvert the LFM radar waveform by O/E conversion in a PD, to the RF frequency of 9.7 GHz. Then, the signal is boosted by a high-power amplifier, filtered by a BPF, and transmitted by a horn Vivaldi antenna. A similar antenna is employed to receive the back-scattered echoes, which are amplified, filtered, and E/O converted by feeding them into the RF port of a MZM, which modulates the second group of modes that is sent back to the CU. Here, the optical signal containing the received echoes is downconverted back to IF by O/E conversion, thanks to narrow-band PDs. At this point, after low-pass filtering, it is acquired by electronic ADCs.

The radar LFM pulses are transmitted in time diversity by TX1 and TX2, with the following waveform parameters: 9.7 GHz carrier frequency; 100 MHz bandwidth (corresponding to a range resolution of 1.5 m); 100 ns pulse duration; 50 µs pulse repetition interval (PRI). The two transmitted waveforms are separated in the time domain with an optical delay line (ODL) implemented by a 1.1 km of SMF, on the path between the CU and RP2. The network is deployed according to the scheme in Fig. 12, with the four antennas aligned over a 21 m long baseline. These are oriented upwards, to mitigate any possible clutter and multipath returns due to the surrounding metal structures, buildings and vegetation. The output power from the TX antennas is 100 mW.

The proposed system has been operated in a preliminary

Copyright (c) 2020 IEEE. Personal use is permitted. For any other purposes, permission must be obtained from the IEEE by emailing pubs-permissions@ieee.org.

This is the author's version of an article that has been published in this journal. Changes were made to this version by the publisher prior to publication.
The final version of record is available at http://dx.doi.org/10.1109/JLT.2020.2989618

outdoor scenario for detecting two collaborative closely spaced targets. These consist of two cylinders, with about 17 cm radius and 50 cm height, made of a tight-mesh metal net. They are carried by two commercial mini-drones, as sketched in Fig. 12. The height of the two targets is controlled and kept between 15 and 20 m, while the two drones keep hovering at the same height, although separated by a cross-range distance of 3 m, to avoid any possible collision.

Results of the normalized ambiguity functions for a single radar channel, are depicted in Fig. 13 a). As we can observe, when one radar bistatic channel is employed, it is not possible to provide azimuth (i.e., cross-range) information about the targets. A simple fusion strategy between all the channel consists in the non-coherent MIMO processing. When talking about MIMO radar centralized architectures, two processing approaches can be applied: non-coherent or coherent [61]. Let us consider a system composed by M transmit and N receive elements. In both cases, all the MxN available signals undergo matched filtering (MF), whose output allows to estimate the distance of a given target. In the first approach, the amplitudes the MF outputs are combined together in such a way that the distance-to-target estimation provides a relatively coarse 2D position estimation [61]. However, a higher accuracy is possible with the second approach. Here, the complex MF outputs are combined together, taking into account also the phase terms due to round-trip propagation, in such a way that the signals add up constructively only at the target location. However, this operation requires precise phase synchronization among all the radar channels. As remarked in [61], the accuracy of this method surpasses the limits imposed by the antenna aperture and signal BW, theoretically allowing to achieve values down to the carrier wavelength. Non-coherent processing is the solution typically employed when the radar architecture can grant only time synchronization among the radar channels, and it provides coarse azimuth information about the targets, since the angular resolution would just correspond to the antenna aperture. However, even in fully coherent radar network, since the coherent MIMO processing is more time-consuming and demanding in terms of computing resources, these systems normally survey the observed area applying the incoherent processing to the acquired data. When a detection is declared, the system focuses the coherent processing to the data related to a small area containing the possible targets, in high-resolution mode [61], providing much better spatial resolution. This adaptive behavior allows for an optimization in the performance, since it enables accurate target detection, at the same time saving system resources.

The output of the non-coherent MIMO processing is depicted in Fig. 13 b). As we can observe, the two targets are too close to be correctly separated along the cross-range dimension, using this processing approach. A single peak of the ambiguity function is distinguishable. The two targets can be separated in cross-range only by applying coherent MIMO processing to the data, as shown in Fig. 13 c). This processing, which is equivalent to a beamforming operation employed on a sparse array of antennas, is possible only when the radar network architecture ensures the adequate level of time and phase synchronization, which is precisely the case of a distributed radar network based on photonic technology, as discussed in [73]. At the best of our knowledge, only photonics may grant the necessary level of diversity in both the spatial and frequency domains by employing one single photonic core in the CU. Given the distance from the baseline of 18 m and the 50° antenna aperture, the expected monostatic cross-range resolution should be about 15.7 m. In terms of target detection and localization performance, with respect to the nominal aperture of the antenna, the cross-range resolution has been improved by a factor > 5, since the two 3 m separated targets are correctly resolved.

It is important to observe the presence of side peaks in the

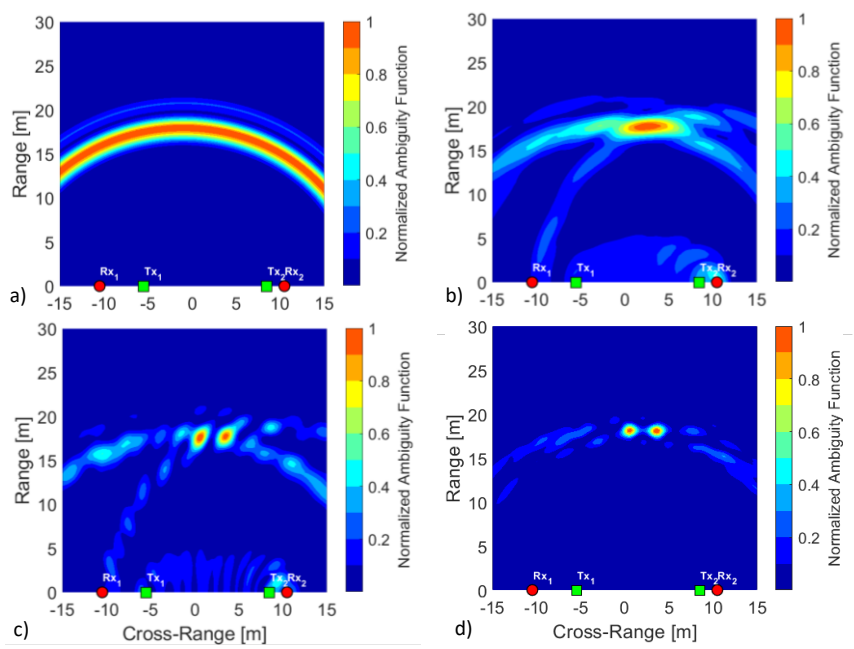

Fig. 13: Normalized ambiguity function at the varying of range and cross range. a) single channel output; b) single-band, noncoherent MIMO processing output; c) single-band, coherent MIMO processing output; d) dual band (X+S bands), simulated coherent MIMO processing output.

Copyright (c) 2020 IEEE. Personal use is permitted. For any other purposes, permission must be obtained from the IEEE by emailing pubs-permissions@ieee.org.

This is the author's version of an article that has been published in this journal. Changes were made to this version by the publisher prior to publication.
The final version of record is available at http://dx.doi.org/10.1109/JLT.2020.2989618

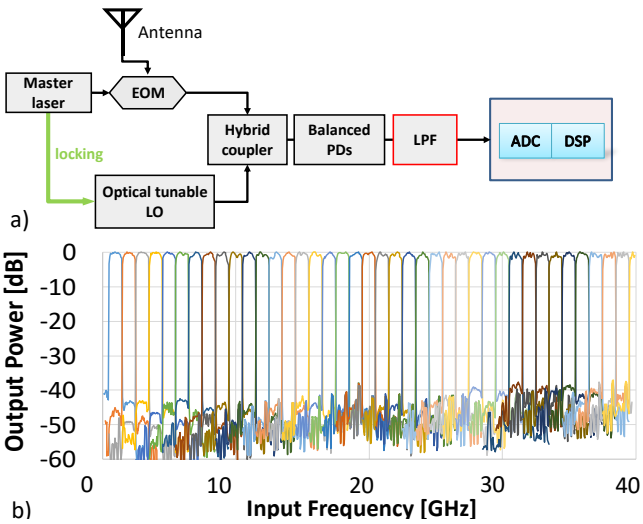

Fig. 14: a) Building blocks architecture of the photonics-assisted RF spectrum scanner; b) received channelized spectrum on the 0.5 – 40.5 GHz range.

ambiguity function (in light blue), in addition to the target-originated ones. They can have a detrimental effect on the system performance, since they can be mistaken for other real targets, giving rise to false alarms. Indeed, a detection is declared where the ambiguity function peaks trespass the detection threshold. Their presence can be not only due to clutter and multipath, but also to the limited number of antennas (i.e. insufficient space diversity) employed by the MIMO radar system, which may lead to additional secondary lobes. These results suggest that a viable solution to reduce unwanted side lobes is to increase the number of virtual channels. This can be done either by increasing the number of TXs and RXs, or by adding other transmission carrier frequencies. Differently from Fig. 13 a) – c), which report experimental results, Fig. 13 d) shows the result of a simulation performed in the case of frequency diversity: here, the transmission and reception of two identical waveforms, in X (9.7 GHz) and S (2.9 GHz) bands is simulated in the same scenario of the outdoor experiment. A better side lobes suppression is achieved, thus diminishing the risk of false alarms, at the same time obtaining a slightly better accuracy in target localization. These simulation results have been obtained without taking into account the possible complex electromagnetic interaction between the two targets, and they must be confirmed by in-field experiments. Nevertheless, they are very promising since they indicate, in principle, the possibility of overcoming the problem of rising sidelobes in this kind of radar systems.

B. The Photonics-Assisted RF Scanner

RF spectrum scanning is a fundamental operation in the domain of electronic support measures (ESM). Indeed, it allows sensing if there is any RF transmission in an analyzed frequency range. In the electronic domain, this operation would require a filter bank, i.e. several parallel physical channels, each filtering a limited portion of the entire spectrum. The MWP system reported in [45], on the other hand, can actually scan the entire RF spectrum from 500 MHz to 40.5 GHz, dividing it in 1-GHz large slices. Fig. 14 a) reports the basic idea of the proposed architecture. A master laser is modulated, on one arm, by the whole received spectrum, whereas it is employed on the other arm to obtain an optical tuneable LO. This block derives a 1 GHz-spaced OFC from the master laser, by cascading amplitude and phase modulators driven by a single frequency electronic oscillator. Then, a distributed feedback (DFB) laser (slave laser), without internal isolator, is fed by the OFC via a circulator. This way, the comb injects the DFB laser, making the latter emit at the closest comb line frequency, being phase locked with it, provided that the comb line falls in the DFB locking range. In other words, by shifting the comb center frequency, which is achieved by tuning the master laser, it is possible to shift, by 1-GHz steps, the entire OFC over the DFB laser, and extract one mode out of the comb. The extracted mode is coupled together with the signal obtained by modulating the master laser with the whole RF spectrum in the upper arm into a 90° hybrid optical coupler. The outputs of the hybrid coupler are photodetected by two balanced PDs. In the PDs, the extracted comb line, detuned from the original master laser, is heterodyned with the whole spectrum and two anti-aliasing low-pass filters (LPFs) isolate the 500 MHz-wide I and Q components. After digitization in two ADCs, the complex 1GHz-bandwidth signal is calculated. This way, by tuning the master and keeping fixed the slave laser, the frequency detuning between the two is changed by 1-GHz steps, making possible the downconversion of all the spectrum in 1 GHz-wide channels, as reported in Figure 14 b). In [45] the developed prototype is widely detailed, and are reported the main metrics of the system, such as the image rejection > 45 dB, the inter-channel crosstalk < -35 dB, and the tuning speed of 10 µs. It is apparent that the proposed architecture has pushed the state of the art very close to the next-future requirements, or even to a better level.

IV. Conclusions

Microwave Photonics may represent, nowadays, a mean for RF systems to reach unprecedented performance, overcoming some inherent limitations of electronic technologies. Many efforts in research and development demonstrated that the coherence guaranteed by photonics can pave the way to a new generation of systems, in communications as well as in the remote sensing field. The latter, in particular, is gradually moving from the strictly military field to our everyday life, with many highly demanding applications in terms of performance and flexibility. MWP is the technology that can help meeting these demands. The MWP basic concept have being exposed always with an eye open on physically implemented subsystems and systems and their performance. The results presented in this paper give a hint of the impact that photonics may have on the implementation next-generation remote sensing systems, such as coherent centralized MIMO radars, opening the possibility to the design and development of radar networks with unprecedented accuracy, reliability, and imaging capabilities.

However, for MWP to become a credible competitor with electronics on a large scale, it is important to push forward the capabilities of obtaining integrated MWP systems and subsystems. As a fact, the latest advances in photonic integration are driving MWP to a turning point in reducing

Copyright (c) 2020 IEEE. Personal use is permitted. For any other purposes, permission must be obtained from the IEEE by emailing pubs-permissions@ieee.org.

This is the author's version of an article that has been published in this journal. Changes were made to this version by the publisher prior to publication.
The final version of record is available at http://dx.doi.org/10.1109/JLT.2020.2989618

SWaP-C, at the same time further enhancing the achievable performance. Every MWP building block or subsystem has been or can be realized as a PIC. Two main integration platforms emerged in the last years. On one hand, the C-MOS compatible technology based on silicon or germanium and its compounds (as Si, Ge, SiO_2, Si_3N_4) allowing for the realization of passive optical (e.g., low-loss waveguides, filters, couplers) or opto-electronic devices (modulators, PDs). On the other hand, the platform based on III-V elements and their compounds (e.g., InP, InGaAs, InGaAsP), can implement optical active (amplifiers, lasers) and electro-optical devices (modulators, photodetectors). Since no single platform can implement, with optimum performance, all the functional blocks needed in a PIC, techniques for hybrid integration of III-V compounds on Si have been largely investigated and developed to exploit the advantages of both technologies [94]. As a matter of fact, photonic integration is the key to allow MWP meeting the market requirements and becoming really competitive with classic electronic devices.

REFERENCES

[1] J. Capmany, D. Novak "Microwave photonics combines two worlds," *Nat. Photonics* 1, pp. 319–330, (2007).
[2] I. Hayashi, M. B. Panish, P.W. Foy, S. Sumski, "Junction Lasers Which Operate Continuously at Room Temperature", *Appl. Phys. Lett.* 17 (3), pp. 109 – 111 (1970).
[3] H. Melchior, "Detectors for lightwave communication," *Physics Today,* 30 (11), pp. 32–39 (1977).
[4] J.B. MacChesney, P.B. O'Connor, H.M. Presby, "A new technique for the preparation of low-loss and graded-index optical fibers," in *Proc. of the IEEE*, 62 (9), pp. 1280-1281 (1974).
[5] E.W. Martin, "A new waveguide switch/modulator for integrated optics", *Appl. Phys. Lett.,* 26 (10), pp. 562-564 (1975).
[6] W.L. Glomb, "Fiber Optic Links for Antenna Remoting", *SPIE 1073*, pp. 523-527 (1992).
[7] W. Ng, A.A. Walston, G.L. Tangonan, J.J. Lee, I.L. Newberg, N. Bernstein, "The first demonstration of an optically steered microwave phased array antenna using true-time-delay," *J. of Light. Techn.*, 9 (9), pp. 1124-1131 (1991).
[8] R.F. Kalman, J.C. Fan, L.G. Kazovsky, "Dynamic range of coherent analog fiber-optic links," *J. of Light. Techn.*, 12 (7), pp. 1263–1277 (1994).
[9] C. Cox, E. Ackerman, R. Helkey, G.E. Betts, "Direct-detection analog optical links," *IEEE Trans. Microw. Theory Tech.*, 45 (8), pp. 1375–1383 (1997).
[10] A. Ramaswamy *et al.*, "Integrated Coherent Receivers for High-Linearity Microwave Photonic Links," *J. of Light. Techn.*, 26 (1), pp. 209–216 (2008).
[11] M. Emmaeinna *et al.*, "Performance analysis of Radio-over-Fiber based on Phase-Modulation and Direct-Detection for the future 5G network", *20th Intern. Conf. on Transp. Opt. Networks (ICTON)*, Bucharest, Romania, (2018).
[12] A. Kabalan *et al.*, "Millimeter-wave home area network prospect with cost-effective RoF links", *Opt. and Quantum Electronics*, Springer US (2019).
[13] E.W. Jacobs *et al.*, "Optically clocked track-and-hold for high-speed high-resolution analog-to-digital conversion," 2004 *IEEE Intern. Topical Meet. on Microw. Phot.*, Ogunquit, ME, pp. 190-192 (2004).
[14] R. Walden, "Analog-to-Digital Conversion in the Early Twenty-First Century", *Wiley Encyclop. of Computer Science and Engin.*, (2008).
[15] H. Gevorgyan, A. Khilo, "Photonic analog-to-digital conversion scheme using an array of optical modulators," *2015 Optoelect. Global Conf. (OGC)*, Shenzhen, PRC, pp. 1-2 (2015).
[16] F.X. Kärtner, A. Khilo, A. H. Nejadmalayeri, "Progress in photonic analog-to-digital conversion," *2013 Opt. Fiber Comm. Conf. & Expo. and Nat'l Fiber Opt. Engin. Conf. (OFC/NFOEC)*, Anaheim, CA, pp. 1-3 (2013).
[17] S. Preußler, G.R. Mehrpoor, T. Schneider, "Frequency-time coherence for all-optical sampling without optical pulse source", *Scientific Reports* 6, Article number: 34500 (2016).
[18] F. Laghezza, F. Scotti, P. Ghelfi, A. Bogoni, S. Pinna, "Jitter-limited photonic analog-to-digital converter with 7 effective bits for wideband radar applications," *2013 IEEE Radar Conference (RadarCon13)*, Ottawa, ON, pp. 1-5 (2013).
[19] M.A. Piqueras, P. Villalba, J. Puche, J. Martí, "High performance photonic ADC for space and defence applications," *2011 IEEE Intern. Conf. on Microw., Comm., Antennas and Elec. Syst. (COMCAS 2011)*, Tel Aviv, 2011, pp. 1-6 (2011).
[20] A. Khilo *et al.*, "Photonic ADC: overcoming the bottleneck of electronic jitter," *Opt. Expr.,* 20 (4), 4454-4469 (2012).
[21] A.M. Fard, S. Gupta, B. Jalali, "Photonic time-stretch digitizer and its extension to real-time spectroscopy and imaging", *Laser Photonics Rev.*, 7 (2), pp. 207-263 (2013).
[22] S. Xu, X. Zou, B. Ma, J. Chen, L. Yu, W. Zou, "Deep-learning-powered photonic analog-to-digital conversion," *Light Sci. Appl.,* 8 (66) (2019).
[23] G.K. Gopalakrishnan, W.K. Burns, C.H. Bulmer, "Microwave-optical mixing in $LiNbO_3$ modulators," in *IEEE Trans. on Microw. Theory and Techn.*, 41 (12), pp. 2383-2391 (1993).
[24] S.R. O'Connor, M.C. Gross, M.L. Dennis, T.R. Clark, "Experimental demonstration of RF photonic downconversion from 4–40 GHz," *2009 Intern. Topical Meeting Micr. Phot. (MWP)*, Valencia (ES), pp. 1-3 (2009).
[25] S. Li, X. Zheng, H. Zhang, B. Zhou, "Highly linear millimeter-wave over fiber transmitter with subcarrier upconversion," *2011 Laser Science to Phot. Appl. (CLEO)*, Baltimore, MD, pp. 1-2 (2011).
[26] P. Ghelfi, G. Serafino, F. Scotti, F. Laghezza, A. Bogoni, "Flexible receiver for multiband orthogonal frequency division multiplexing signals at the millimeter waveband based on optical downconversion," *Opt. Lett.* 37 (18), pp. 3924-3926 (2012).
[27] E.H.W. Chan, R.A. Minasian, "Microwave Photonic Downconverter with High Conversion Efficiency," in *J. of Lightw. Techn.*, 30 (23), pp. 3580-3585 (2012).
[28] D. Zhu, S. Pan, "Photonics-Based Microwave Image-Reject Mixer" *Photonics 2018*, 5 (2), 6 (2018).
[29] P. Ghelfi, F. Scotti, A.T. Nguyen, G. Serafino, A. Bogoni, "Novel Architecture for a Photonics-Assisted Radar Transceiver Based on a Single Mode-Locking Laser," *IEEE Phot. Techn. Lett.*, 23 (10), pp. 639-641 (2011).
[30] X.S. Yao, L. Maleki, "Optoelectronic microwave oscillator", *J. of the Opt. Soc. of America B,* 13 (8), pp. 1725-1735 (1996).
[31] V. Torres-Company, A. M. Weiner, "Optical frequency comb technology for ultra-broadband radiofrequency photonics," *Laser Photonics Rev.* 8 (3), pp. 368–393 (2014)
[32] A. Liu, J. Dai, K. Xu, "Stable and Low-Spurs Optoelectronic Oscillators: A Review", *Appl. Science*, 8, 2623 (2018).
[33] D.T. Spencer *et al.*, "An optical-frequency synthesizer using integrated photonics", *Nature* 557, pp. 81–85 (2018).
[34] M. Lu *et al.*, "A highly-integrated optical frequency synthesizer based on phase-locked loops," *2014 Opt. Fiber Comm. Conf. & Expo. and Nat'l Fiber Opt. Engin. Conf. (OFC/NFOEC)*, San Francisco, CA, pp. 1-3 (2014).
[35] J. Capmany, B. Ortega, D. Pastor, "A Tutorial on Microwave Photonic Filters," *J. of Lightw. Techn.*, 24 (1), 201-229 (2006).
[36] J. Capmany, J. Mora, I. Gasulla, J. Sancho, J. Lloret, S. Sales, "Microwave Photonic Signal Processing," *J. of Lightw. Techn.*, 31 (4), 571-586 (2013).
[37] V.R. Supradeepa *et al.*, "Comb-based radiofrequency photonic filters with rapid tunability and high selectivity" *Nature Phot.,* 6 (3), pp. 186–194 (2012).
[38] J. Palací, G.E. Villanueva, J.V. Galan, J. Martí, B. Vidal, "Single bandpass photonic microwave filter based on a notch ring resonator," *IEEE Photon. Technol. Lett.,* 22 (17), pp. 1276–1278 (2010).
[39] M.A. Popovíc *et al.*, "Multistage high-order microring-resonator add-drop filters," *Opt. Lett.*, 31 (17), pp. 2571-2573 (2006).
[40] C. Porzi, G. Serafino, P. Velha, P. Ghelfi, A. Bogoni, "Integrated SOI High-Order Phase-Shifted Bragg Grating for Microwave Photonics Signal Processing," *J. of Lightw. Techn.*, 35 (20), 4479-4487 (2017).
[41] C. Taddei *et al.*, "Fully reconfigurable coupled ring resonator-based bandpass filter for microwave signal processing," *9th Asia-Pacific Microw. Phot. Conf. (APMC)*, Sendai, Japan, pp. 44-47 (2014).
[42] M.S. Rasras *et al.*, "Demonstration of a Fourth-Order Pole-Zero Optical Filter Integrated Using CMOS Processes," *J. of Lightw. Techn.*, 25 (1), pp. 87-92 (2007).
[43] P. Dong *et al.*, "GHz-bandwidth optical filters based on high-order silicon ring resonators," *Opt. Expr.,* 18 (23), pp. 23784-23789 (2010).

Copyright (c) 2020 IEEE. Personal use is permitted. For any other purposes, permission must be obtained from the IEEE by emailing pubs-permissions@ieee.org.

This is the author's version of an article that has been published in this journal. Changes were made to this version by the publisher prior to publication.
The final version of record is available at http://dx.doi.org/10.1109/JLT.2020.2989618

[44] C. Porzi, G.J. Sharp, M. Sorel, A. Bogoni, "Silicon Photonics High-Order Distributed Feedback Resonators Filters," *IEEE J. of Quant. El.*, 56 (1), pp. 1-9 (2020).
[45] P. Ghelfi, F. Scotti, D. Onori, A. Bogoni, "Photonics for Ultrawideband RF Spectral Analysis in Electronic Warfare Applications," *IEEE J. Sel. Topics Quant. Electr*., 25 (4), pp. 1-9 (2019).
[46] L. Zhuang *et al.*, "Novel ring resonator-based integrated photonic beamformer for broadband phased array receive antennas—Part II: Experimental prototype," *J. of Lightw. Techn.,* 28 (1), pp. 19-31 (2010).
[47] P. Ghelfi *et al.*, "Photonic generation and independent steering of multiple RF signals for software defined radars", *Opt. Expr.* 21 (19), pp. 22905-22910 (2013).
[48] C. Roeloffzen *et al*., "Enhanced coverage though optical beamforming in fiber wireless networks," *19th Intern. Conf. on Transp. Opt. Networks (ICTON)*, Girona, Spain, pp. 1-4 (2017).
[49] V.J. Urick *et al.*, "Microwave Phase Shifting Using Coherent Photonic Integrated Circuits," *IEEE J. Sel. Topics Quant. Electr*., 22 (6), pp. 353-360 (2016).
[50] G. Serafino *et al*., "Photonics-Assisted Beamforming for 5G Communications," *IEEE Phot. Techn. Lett.*, 30 (21), pp. 1826-1829 (2018).
[51] C. Porzi *et al.*, "Photonic Integrated Microwave Phase Shifter up to the mm-Wave Band With Fast Response Time in Silicon-on-Insulator Technology," *J. of Lightw. Techn.,* 36 (19), pp. 4494-4500 (2018).
[52] B. Hussain *et al.*, "Fast Photonics-Assisted Beamforming Network for Wide-Band, High Bit Rate 5G Communications," *2018 Intern. Topical Meeting on Microw. Phot. (MWP)*, Toulouse, France, pp. 1-4 (2018).
[53] P. Wu, S. Tang, D. Raible, "A prototype high-speed optically-steered X-band phased array antenna," *Opt. Expr.*, 21 (16), pp. 32599-32604 (2013).
[54] X. Ye, F. Zhang, S. Pan, "Compact optical true time delay beam-former for a 2D phased array antenna using tunable dispersive elements," *Opt. Lett.*, 41 (17), pp. 3956-3959 (2016).
[55] G. Serafino *et al*., "A Photonic Beamforming Network Based on Phase Shifters for Microwave Wide-Band Applications," *21st Intern. Conf. on Transp. Opt. Networks (ICTON)*, Angers, France, pp. 1-4 (2019).
[56] D. Marpaung, C. Roeloffzen, R. Heideman, A. Leinse, S. Sales, J. Capmany, "Integrated microwave photonics," *Laser Photonics Rev.* 7, pp. 506–538 (2013).
[57] M. Smit, K. Williams, J. van der Tol, "Past, present, and future of InP-based photonic integration," *APL Photonics*, 4 (5) (2019).
[58] R. Maram, S. Kaushal, J. Azaña, L. Chen, "Recent Trends and Advances of Silicon-Based Integrated Microwave Photonics," *Photonics 2019*, 6 (1), 13, MDPI (2019).
[59] C.G.H. Roeloffzen, "Silicon nitride microwave photonic circuits," *Opt. Expr.,* 21 (19), pp. 22937-22961 (2013).
[60] L. Carroll *et al.*, "Photonic Packaging: Transforming Silicon Photonic Integrated Circuits into Photonic Devices," *Appl. Sciences*, 6 (12), p. 426 (2016).
[61] A.M. Haimovich, R.S. Blum, L.J. Cimini, "MIMO Radar with Widely Separated Antennas," *IEEE Sign. Proc. Mag.*, 25 (1), pp. 116-129 (2008).
[62] I. Bekkerman, J. Tabrikian, "Target detection and localization using MIMO radars and sonars," *IEEE Trans. on Signal Proc.*, 54 (10), pp. 3873-3883, Oct. 2006.
[63] H. Godrich, A.M. Haimovich, R.S. Blum, "Target Localization Accuracy Gain in MIMO Radar-Based Systems" *IEEE Trans. on Information Theory*, 56 (6), pp. 2783-2803 (2010).
[64] M.S. Greco, J. Li, T. Long, A. Zoubir, "Advances in Radar Systems for Modern Civilian and Commercial Applications: Part 1," *IEEE Signal Proc. Magazine*, 36 (4), pp. 13-15 (2019).
[65] V.S. Chernyak, *Fundamentals of Multisite Radar Systems*. New York: Gordon and Breach (1998).
[66] C.J. Baker, A.L. Hume, "Netted Radar Sensing", *IEEE Aerosp. & Electr. Syst. Magazine*, 18 (2), pp. 3-6 (2003).
[67] T. Derham, S. Doughty, K. Woodbridge, C.J. Baker, "Realisation and Evaluation of a Low Cost Netted Radar System," *2006 CIE Intern. Conf. on Radar*, pp. 1-4, Shanghai, PRC, (2006).
[68] S. Maresca, P. Braca, J. Horstmann, R. Grasso, "Maritime Surveillance Using Multiple High-Frequency Surface-Wave Radars," *IEEE Trans. on Geoscience and Remote Sensing*, 52 (8), pp. 5056-5071 (2014).
[69] A.S. Fletcher, F.C. Robey, "Performance bounds for adaptive coherence of sparse array radar," *11th Conf. on Adapt. Sens. Array Proc.*, Online (2003).
[70] E. Fishler, A. Haimovich, R.S. Blum, L.J. Cimini, D. Chizhik, R.A. Valenzuela, "Spatial diversity in radars – Models and detection performance," *IEEE Trans. on Sign. Proc.*, 54 (3), pp. 823-838 (2006).
[71] P. Ghelfi, F. Laghezza, F. Scotti, D. Onori, A. Bogoni, "Photonics for Radars Operating on Multiple Coherent Bands", *J. of Lightw. Techn.*, 33 (2), pp.500-507 (2016).
[72] P. Ghelfi *et al.*, "A fully photonics-based coherent radar system", *Nature*, 507, pp. 341–345 (2014).
[73] A. Bogoni, P. Ghelfi, F. Laghezza, *Photonics for Radar Networks and Electronic Warfare Systems*, *IET SciTech Publishing*, London (2019).
[74] P.A. Williams, W.C. Swann, N.R. Newbury, "High-stability transfer of an optical frequency over long fiber-optic links," *J. of the Opt. Soc. of America B*, 25 (8), pp. 1284-1293 (2008).
[75] F. Laghezza *et al.*, "Field evaluation of a photonics-based radar system in a maritime environment compared to a reference commercial sensor," *IET Radar, Sonar & Navigation,* 9 (8), pp. 1040-1046 (2015).
[76] L. Lembo *et al.,* "In-field demonstration of a photonic coherent MIMO distributed radar network,"*2019 IEEE Radar Conf.*, Toulon, France (2019).
[77] J. Fu, S. Pan, "A fiber-distributed bistatic ultra-wideband radar based on optical time division multiplexing", *2015 Intern. Topical Meeting Microw. Phot. (MWP)*, Paphos, Cyprus (2015).
[78] T. Yao, D. Zhu, D. Ben, S. Pan, "Distributed MIMO chaotic radar based on wavelength-division multiplexing technology," *Opt. Lett.,* 40 (8), pp. 1631-1634 (2015).
[79] F. Zhang, B. Gao, S. Pan, "Photonics-based MIMO radar with high-resolution and fast detection capability," *Opt. Expr.,* 26 (13), pp. 17529-17540 (2018).
[80] S. Maresca, *et al.,* "Photonics for coherent MIMO radar: an experimental multi-target surveillance scenario," *Intern. Radar Symp. (IRS)*, Bonn, Germany, (2019).
[81] G. Serafino *et al*., "Toward a New Generation of Radar Systems Based on Microwave Photonic Technologies," *J. of Lightw. Techn.*, 37 (2), pp. 643-650 (2019).
[82] M. Endo, T.D. Shoji, T.R. Schibli, "Ultralow Noise Optical Frequency Combs," *IEEE J. Sel. Topics Quantum Electron*., 24 (5), pp. 1-13 (2018).
[83] N. Andriolli, T. Cassese, M. Chiesa, C. de Dios, G. Contestabile, "Photonic Integrated Fully Tunable Comb Generator Cascading Optical Modulators," *J. of Lightw. Techn.*, 36 (23), pp. 5685-5689 (2018).
[84] T. Kawanishi, T. Sakamoto, M. Izutsu, "High-Speed Control of Lightwave Amplitude, Phase, and Frequency by Use of Electrooptic Effect," *IEEE J. Sel. Topics Quantum Electron*., 13 (1), pp. 79-91 (2007).
[85] V.J. Urick, J.D. McKinney, K.J. Williams, *Fundamentals of Microwave Photonics*, Wiley Ed., 2015.
[86] E. Krune, B. Krueger, L. Zimmermann, K. Voigt, K. Petermann, "Comparison of the Jitter Performance of different Photonic Sampling Techniques," *J. of Lightw. Techn.*, 34 (4), pp. 1360-1367 (2016).
[87] T.J. Kippenberg, R. Holzwarth, S.A. Diddams, "Microresonator-based optical frequency combs," *Science* 332, pp. 555–559 (2011).
[88] V. Moskalenko, S. Latkowski, S. Tahvili, T. de Vries, M. Smit, E. Bente, "Record bandwidth and sub-picosecond pulses from a monolithically integrated mode-locked quantum well ring laser," *Opt. Expr.*, 22 (23), pp. 28865-28874 (2014).
[89] G. Serafino *et al.*, "Phase and Amplitude Stability of EHF-Band Radar Carriers Generated from an Active Mode-Locked Laser *J. of Lightw. Techn.*, 29 (23), pp. 3551-3559 (2011).
[90] S.J. Orfanidis, *Electromagnetic Waves and Antennas*, p. 932, Rutgers University (2013).
[91] C.K. Madsen, J.H. Zhao, "Optical Filter Design and Analysis: A Signal Processing Approach," John Wiley & Sons, (1999).
[92] H.A. Haus, Y. Lai, "Theory of cascaded quarter wave shifted distributed feedback resonators," *IEEE J. of Quant. El.*, 28 (1), pp. 205-213 (1992).
[93] R. Jones, J. Doylend, P. Ebrahimi, S. Ayotte, O. Raday, O. Cohen, "Silicon photonic tunable optical dispersion compensator," *Opt. Expr.* 15 (24), pp. 15836-15841 (2007).
[94] J.M. Ramirez *et al*., "III-V-on-Silicon Integration: From Hybrid Devices to Heterogeneous Photonic Integrated Circuits," *IEEE J. Sel. Topics Quant. Electr*., 26 (2), pp. 1-13 (2020).

Copyright (c) 2020 IEEE. Personal use is permitted. For any other purposes, permission must be obtained from the IEEE by emailing pubs-permissions@ieee.org.